

9-10-2010

# Structural assesment of joints in satellites using guided waves

Angela Montoya

Follow this and additional works at: [https://digitalrepository.unm.edu/ce\\_etds](https://digitalrepository.unm.edu/ce_etds)

---

## Recommended Citation

Montoya, Angela. "Structural assesment of joints in satellites using guided waves." (2010). [https://digitalrepository.unm.edu/ce\\_etds/34](https://digitalrepository.unm.edu/ce_etds/34)

This Thesis is brought to you for free and open access by the Engineering ETDs at UNM Digital Repository. It has been accepted for inclusion in Civil Engineering ETDs by an authorized administrator of UNM Digital Repository. For more information, please contact [disc@unm.edu](mailto:disc@unm.edu).

**Angela Cork Montoya**


*Candidate*

**Department of Civil Engineering**

*Department*

This thesis is approved, and it is acceptable in quality and form for publication:

*Approved by the Thesis Committee:*



Arup K. Maji , Chairperson



Hans-Peter Dumm



Walter Gerstle

**STRUCTURAL ASSESSMENT OF JOINTS IN SATELLITES USING  
GUIDED WAVES**

**BY**

**ANGELA C. MONTOYA**

**BACHELORS OF SCIENCE IN PHYSICS  
UNIVERSITY OF NEW MEXICO  
DECEMBER, 2002**

**THESIS**

Submitted in Partial Fulfillment of the  
Requirements for the Degree of  
**Master of Science**

**Civil Engineering**

The University of New Mexico  
Albuquerque, New Mexico

**July, 2010**

## DEDICATION

To my husband, John.

For his encouragement, his enthusiasm, and his endless love.

## ACKNOWLEDGMENTS

I owe a deep debt of gratitude to my advisor Dr. Arup K. Maji for giving me the opportunity to work with him. He gave me direction when I most needed it. His insights were instrumental in this thesis from formation to conclusion.

I am very fortunate to have been allowed to perform experiments on an actual, fully functioning satellite at the Air Force Research Laboratory Space Vehicles Directorate. The opportunity also allowed me to work with some wonderful people at the Air Force Research Laboratory. Mr. Hans-Peter Dumm's support and guidance has been invaluable. I am very grateful for the insight and experience that Mr. Derek Doyle shared with me. While forming test-plans and performing experiments, Mr. Whitney Reynolds made me feel like part of the team. Mr. Dumm and Mr. Doyle were instrumental in the final version of the quality assessment method presented in this thesis.

I deeply appreciate Dr. Walter Gerstle, Mr. Hans-Peter Dumm, and Arup K. Maji for serving on my thesis committee. I would also like to thank Dr. Laura Crossey for her guidance in all things 'graduate school', my fellow graduate students for their understanding and moral support, and my friends and family for their unwavering support and patience.

The Air Force Research Laboratory Space Vehicles Directorate and the National Science Foundation Alliance for Minority Participation Bridge to the Doctorate Fellowship Program funded this research.

**STRUCTURAL ASSESSMENT OF JOINTS IN SATELLITES USING  
GUIDED WAVES**

**BY**

**ANGELA C. MONTOYA**

**ABSTRACT OF THESIS**

Submitted in Partial Fulfillment of the  
Requirements for the Degree of

**Master of Science**

**Civil Engineering**

The University of New Mexico  
Albuquerque, New Mexico

**July, 2010**

# **STRUCTURAL ASSESSMENT OF JOINTS IN SATELLITES USING GUIDED WAVES**

by

**Angela C. Montoya**

**B.S., Physics, University of New Mexico, 2002**

**M.S., Civil Engineering, University of New Mexico, 2010**

## **ABSTRACT**

The intention of the Air Force's Responsive Space Initiative Project is to develop procedures and technologies necessary to produce a satellite within six days from the initial order. Modular satellite designs have been proposed to help streamline the process of preparing a satellite for deployment. These designs would save time by allowing panels with common functions to be manufactured and tested long before a new satellite is needed. Prior to launch, the integrity of the panel-to-panel connections would need to be tested for quality in order to show that the craft is flight worthy. The experimental test method presented in this thesis performs a targeted quality assessment of the connections between satellite panels. The test method is intended for responsive satellites designed with prefabricated and pretested panels for which traditional vibration testing would be redundant. A first investigation of the feasibility of using transmitted wave energy for joint quality assessment was conducted at the University of New Mexico using a simple bolted connection between two aluminum plates. Comparisons were made between wave

energy transmission and a mechanical assessment of the joint rigidity. Results show a correlation between joint rigidity and energy transmission, demonstrating the feasibility of the using wave energy transmission amplitudes to inspect aluminum-to-aluminum dry connected joints. Later experiments were conducted at Air Force Research Laboratory facilities on a fully functional satellite and detached satellite panels. These experiments showed that the test method is able to detect faulty connections with higher fidelity than current satellite testing methods. The experimental setup and methods for each set of experiments is presented along with an overall assessment of the utility of the test method for use with responsive satellites.



## TABLE OF CONTENTS

<b>LIST OF FIGURES.....</b>	<b>XII</b>
<b>LIST OF TABLES.....</b>	<b>XIV</b>
<b>CHAPTER 1: INTRODUCTION .....</b>	<b>1</b>
1.1. Responsive Space Initiative Project .....	1
1.2. Background.....	2
1.2.1. Traditional satellite testing methods.....	2
1.2.2. Current state of the art .....	3
1.3. Motivation for this thesis .....	4
1.4. Scope of this thesis.....	5
<b>CHAPTER 2: BACKGROUND.....</b>	<b>7</b>
2.1. Classification and behavior of ultrasonic waves.....	7
2.1.1. Rayleigh waves.....	8
2.1.2. Lamb waves .....	11
2.2. Use of piezoelectric materials to excite and sense guided waves .....	13
2.2.1. Method of excitation.....	13
2.2.2. Reception of guided waves .....	16
2.3. Reflection and transmission of guided waves.....	17
2.3.1. Current research in wave scattering.....	18
2.3.2. Wave interaction at poorly defined interfaces .....	18
2.4. Current research into ultrasonic inspection of rough interfaces and joints .....	22
2.4.1. Rough interfaces.....	23
2.4.2. Joint inspection in aerospace structures.....	24

2.5.	Summary.....	26
<b>CHAPTER 3: PROOF OF CONCEPT EXPERIMENT.....</b>		<b>28</b>
3.1.	Intent and goals of the experiment .....	28
3.2.	Sample joint .....	28
3.3.	Sensors.....	29
3.3.1.	Placement of the sensors.....	29
3.3.2.	Dynamic behavior and resonance of piezoelectric sensors.....	31
3.4.	Mechanical assessment of joint rigidity .....	33
3.4.1.	Characterization of the joint between two extreme cases.....	34
3.4.2.	Deflection measurement set-up.....	36
3.4.3.	Deflection measurement procedure .....	39
3.5.	Measurement of wave energy transmission.....	40
3.5.1.	Equipment and LabView™ programming.....	40
3.5.2.	Procedure .....	41
3.5.3.	Calculation of energy parameter $E_j$ .....	42
3.6.	Results and analysis .....	44
3.6.1.	Results of the mechanical joint assessment .....	44
3.6.2.	Linearity of the system .....	45
3.6.3.	Correlation in $E_j$ with the joint rigidity ratio.....	47
3.6.4.	Summary of results .....	50
<b>CHAPTER 4: EXPERIMENTS CONDUCTED ON SATELLITE.....</b>		<b>51</b>
<b>PNP 1.....</b>		<b>51</b>
4.1.	Goals of the experiment.....	51
4.2.	Equipment and Test Subject .....	52

4.3.	Transmitted energy parameter $E_r$ .....	53
4.3.1.	New experimental parameters.....	54
4.3.2.	Equation.....	56
4.4.	Procedure.....	57
4.4.1.	First phase of the experiment: craft held stationary.....	59
4.4.2.	Second phase of the experiment: craft perturbed by vibration.....	60
4.5.	Results and discussion.....	60
4.5.1.	Phase one: craft held stationary.....	60
4.5.2.	Phase two: craft perturbed by vibration.....	63
4.5.3.	Summary of results.....	64
<b>CHAPTER 5: EXPERIMENTS CONDUCTED ON SATELLITE PNP2 .....</b>		<b>66</b>
5.1.	Goals of the experiment.....	66
5.2.	PnP 2 panels and location of sensors.....	66
5.3.	Procedure.....	70
5.3.1.	Repeatability tests.....	70
5.3.2.	Range tests.....	71
5.4.	Results and discussion.....	72
5.4.1.	Short-term repeatability.....	72
5.4.2.	Long-term repeatability.....	75
5.4.3.	Range.....	76
5.4.4.	Summary of results.....	80
<b>CHAPTER 6: CONCLUDING REMARKS.....</b>		<b>82</b>
6.1.	Proof of concept experiment allowed the project to move forward.....	82
6.2.	These Responsive Space Initiative Project goals were met by experiments done on PnP1 and PnP2.....	82

6.3. Future work.....	84
<b>REFERENCES .....</b>	<b>82</b>
<b>APPENDIX 1: MATHEMATICA CODE USED TO PRODUCE LAMB WAVE DISPERSION CURVES.....</b>	<b>90</b>
<b>APPENDIX 2: MATERIAL DATA FOR PIEZOSYSTEMS PSI-5A4E (51) .....</b>	<b>95</b>
<b>APPENDIX 3: DOCUMENTATION FOR LABVIEW PROGRAMS.....</b>	<b>97</b>
<b>APPENDIX 4: DERIVATION OF JOINT RIGIDITY EQUATION.....</b>	<b>102</b>
<b>APPENDIX 5: SUMMARY OF RITEC DOCUMENTATION FOR THE INTEGRATOR CIRCUIT .....</b>	<b>105</b>
<b>APPENDIX 6: PANEL AND BRACKET DIMENSIONS FOR PNP 2 .....</b>	<b>107</b>

## LIST OF FIGURES

Figure 1: Image of a satellite panel with embedded components. ....	1
Figure 2: Two-dimension plate with thickness $2d$ . ....	9
Figure 3: Mode shapes for symmetric and anti-symmetric lamb waves. ....	12
Figure 4: Dispersion curves for the first Lamb wave modes. ....	13
Figure 5: Shearing perturbations that produce guided waves. ....	14
Figure 6: Definition of interfacial stiffness from Baik and Thompson.. ....	22
Figure 7: Back and side view of the sample joint. ....	29
Figure 8: Front and side view of the sample joint showing the placement of the sensors. ....	30
Figure 9: Bonding of the sensors to the plate.....	31
Figure 10: Idealization of model joint. ....	34
Figure 11: A beam with one end pinned.....	34
Figure 12: A beam with one end fixed . ....	35
Figure 13: Back and Side view of joint attached to a steel plate. ....	36
Figure 14: : Photograph of the back view of the test sample.....	37
Figure 15: Top down view of the experiment.....	38
Figure 16: Raw data collected at sensor pair HIV1.....	42
Figure 17: Plot of $E_j$ values against joint rigidity ratio values for each sensor pair.....	47
Figure 18: Location of sensors and actuators on the spacecraft.....	52
Figure 19: The red line represents the input signal at actuator 4T.....	54
Figure 20: The bracket assembly contained 13 bolts. ....	58
Figure 21: Panels designated PnP2.....	67
Figure 22: Diagram of the PnP 2 satellite panels showing the bracket layout.....	67

Figure 23: Bracket one as seen from the back side of the panel. ....	68
Figure 24: Bolt numbering scheme for Bracket one. ....	68
Figure 25: Location of the sensors. ....	69
Figure 26: Repeatability for Bolt 13.....	74
Figure 27: Values from Table 11 plotted in order taken. ....	75
Figure 28: Change in energy by a single loose bolt. ....	77
Figure 29: Energy change with loose bolts.....	78
Figure 30: View of the vertical plane.. ....	102
Figure 31: Horizontal plane, top-down view. ....	103
Figure 32: Close in view of the horizontal plane. ....	103
Figure 33: PnP 2 Bracket geometry.....	107
Figure 34: Sensors placed near bracket 1.. ....	107

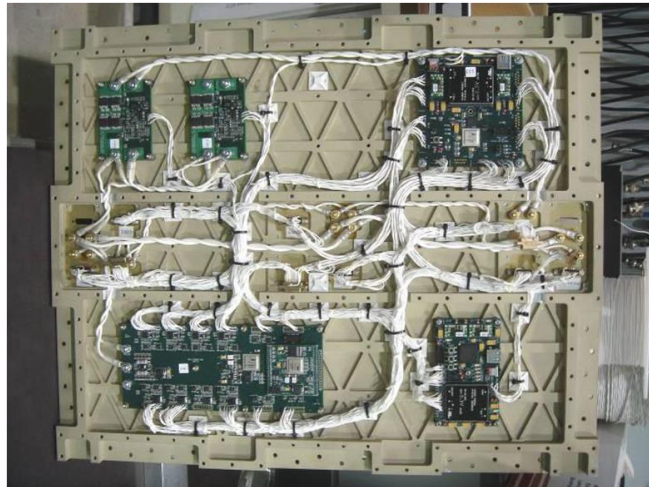
## LIST OF TABLES

Table 1: Material values for 6000 series aluminum .....	8
Table 2: Mechanical assessment of the joint.....	45
Table 3: $R^2$ values for each least-squares analysis performed .....	46
Table 4: Correlation statistics by sensor pair between $E_j$ values and joint rigidity ratios	49
Table 5: $E_r$ values after loosening and returning the bolts to design specification .....	61
Table 6: Variation in $E_r$ by gate widths for the 1.8 Nm preload test-case .....	61
Table 7: $E_r$ values for all three sensor paths for a 50 $\mu$ s gate setting.....	62
Table 8: Variation in baseline E values detected. ....	63
Table 9: Sensor pair 4T-1 with a 50 $\mu$ s gate duration.....	63
Table 10: Horizontal distance from each bolt to the sensors. ....	70
Table 11: Energy values (E) for each bolt number.....	73
Table 12: Energy values for the bracket when all 18 bolts were adjusted.....	79
Table 13: $E_r-1$ for each bolt as it was loosened to a variable torque.....	80

## CHAPTER 1: INTRODUCTION

### 1.1. Responsive Space initiative

The intention of the Air Force's Responsive Space initiative is to develop procedures and technologies necessary to produce a satellite within six days from the initial order. Currently, the process for a satellite to reach deployment from conception may take months to years (1). This prolonged length of time can undermine a time dependent mission or render the system technologically obsolete prior to launch. As a result, current trends in satellite design are tending towards more efficient, modular forms. Spacecraft must be proven flight worthy with a battery of tests before deployment (2). Modular designs save time by pre-assembling and pre-testing body panels with generic functions, like the panel shown in Figure 1, before the satellite is ordered for service.



**Figure 1: Image of a satellite panel with embedded components. Panels such as these would have generic functions that most satellites would need.**



Prior to launch, the integrity of the panel-to-panel connections would need to be tested in order to show that the craft is flight worthy.

## **1.2. Background**

As discussed by B.B. Arritt et al. in their paper “Responsive Satellites and the Need for Structural Health Monitoring”(1), the fields of Structural Health Monitoring (S.H.M.) and Non-destructive Evaluation (N.D.E.) contain many promising techniques for use as a panel-to-panel evaluation method. Any panel-to-panel test suggested should improve the existing pre-flight testing process.

### **1.2.1. Traditional satellite testing methods**

Current structural assessments of satellites are done by shock and random vibration testing. The primary purpose of these tests is to assess the connections and verify the fundamental frequency of the craft (2). Panel-to-panel connections are designed with redundant fasteners. Unfortunately, vibration testing cannot detect a loose connection that does not affect the global stiffness of the craft, so a single loose fastener could go unnoticed with traditional shock and vibration testing (1). If a loose connection is detected by vibration testing, the loose connection is made evident as some change in the global response to vibration. Since the location of damage is unspecified, the testing engineers have no way of knowing where the loose connection is located. Often the craft has to be completely disassembled and then reassembled to fix the damage (1). While an additional test adds to the existing testing regime, quickly finding a loose connection is valuable.

### 1.2.2. Current state of the art

A variety of techniques exists in the fields of Non-Destructive Evaluation and Structural Health Monitoring for aerospace structures with guided ultrasonic waves (3). Most research has concentrated on finding fatigue cracks in panel interiors. Investigations done on joints are primarily lap-style joints that are made by an adhesive bond between two pieces of material such as work done by Challis et al. and Puthillath et al. (4), (5) or machined out of a solid piece of material such as the work done by Song, Rose and Galan (6). Doyle et al. (7) and Lovell et al. (8) have investigated joints by observing changes in phase in a wave propagating parallel to the joint interface due to changes in the elastic properties of the medium. The literature review for this thesis concentrates on previous research into ultrasonic measurements of dry connections. For the purposes of this thesis, a dry connected joint is defined as a joint that does not have any kind of adhesive or acoustic couplant between members. Solutions for ultrasonic wave transmission problems require fully specified boundary conditions (3). Loose or roughly connecting interfaces in joints are poorly defined boundaries by definition; making evaluation of these interfaces by wave transmission problematic. Yet, there have been several attempts using various analytic models for the rough connection. Dryer-Joyce et al. (9) used ultrasound to investigate a roughly contacting interface in the context of detecting cracks. The model they used was the quasi-static 'spring model' developed by Baik and Thompson (10). Dryer-Joyce et al. was able to show a correlation between contact stiffness and the reflection coefficient two to three orders of magnitude more sensitive than from load deflection measurements. Similar research by Lavrentyev and

Rokhlin (11) in the field of contact mechanics shows reflected wave amplitudes from rough interfaces decreasing with decreased stress at the interface.

Guided waves are popular in Structural Health Monitoring because they have lower attenuation rates than other types of waves (3). However, guided waves scatter and undergo complicated mode conversion at any discontinuity encountered in the medium (6). Actual aerospace structures like satellite panels contain many bolt holes, voids, and changes in thickness. For this reason, Dalton et al. (12) suggested that guided wave analysis of more complicated aerospace structures, such as joints, are most effective when used with a short range. By testing the interface locally, some of the complexity of the surrounding panels may be disregarded, and the need to locate damage by triangulating signals becomes unnecessary. Additionally, by testing a range of frequencies, mode conversions and other guided wave frequency dependent phenomena may be accounted for.

### **1.3. Motivation for this thesis**

A targeted quality assessment of the panel-to-panel connections would be able to detect faulty connections with higher fidelity than current methods and signal the location of a faulty connection to test engineers. Another important consideration is the need to use lightweight sensors. Sensors that could be approved for space flight or used for other types of ultrasonic testing are ideal. Being lightweight, the sensors would have very little impact on the design. Having the versatility to be used for a variety of tests or as in situ monitoring devices further reduces the number of sensors on the craft. Satellite joints are often complex and vary greatly in design. An assessment method would also need to be

easily adaptable to different joint geometry. In summary, the assessment method should target a specific area for a loose connection, be versatile enough to detect damage with different configurations of joints, and be as unobtrusive as possible.

Ultimately, the goal is to eliminate the need for vibration testing by providing a targeted assessment of panel-to-panel connections in a satellite with a modular design. To reach this goal, the ultrasonic joint assessment developed in this thesis utilizes a range of frequencies to account for complicated guided wave scattering and compiles the results into a single parameter that is proportional to the stiffness of the joint. For all experiments, a single pair of piezoelectric wafers are used alternately as transducer and as receiver. They are to opposite panels across a joint in order to assess the joint as a whole. Three sets of experiments are used in the design and evaluation of this assessment method.

#### **1.4. Scope of this thesis**

Before presenting the experiments, background information is given in Chapter 2. Some aspects of guided wave behavior are discussed and a brief description of the piezoelectric sensors used in the experiments is included. The last part of Chapter 2 discusses previous research done with guided waves and joint-like interfaces.

Chapter 3 reports on the initial proof of concept experiment done to test feasibility of using transmitted wave energy for joint quality assessment. Experiments were conducted on a joint consisting of a dry aluminum-to-aluminum connection, similar to possible panel-to-panel connections that could be used as part of a modular satellite

design. Comparisons were made between wave energy transmission and a mechanical assessment of the joint rigidity. Results for five tests cases are presented and discussed.

Chapter 4 describes and discusses experiments performed on a functional satellite, designated PnP 1 (Plug 'n Play 1), at Air Force Research Laboratory facilities. Experiments conducted on a functional satellite were intended to test, in part, the feasibility of deploying this test method under realistic circumstances. An assessment of the method including repeatability of the method is discussed.

Chapter 5 describes and discusses experiments performed on detached satellite panels, designated PnP 2 (Plug 'n Play 2), at Air Force Research Laboratory facilities. This chapter discusses the results of experiments intended to determine the range of the test method, and sensitivity to different parameters.

Finally, chapter 6 concludes this thesis with a summary of results and comments on future work needed to meet the ultimate goals of the Responsive Space Initiative Project.

## CHAPTER 2: BACKGROUND

The purpose of this chapter is to discuss previous research that provided some of the motivation for the joint evaluation technique that was developed for this thesis. The first part of this chapter briefs the reader on specific aspects of physical phenomena involving ultrasonic measurements. The second part of this chapter is a review of current and past research that highlights physical phenomena that could be used in joint evaluation and research that outlines the problems associated with certain methods.

### 2.1. Classification and behavior of ultrasonic waves

Horace Lamb (13) was the first to describe elastic waves that propagate with a wavelength comparable to the thickness of the medium as Rayleigh or Lamb waves. The longitudinal and shear modes for these waves are coupled, and the wave speeds are different from that of bulk waves. These types of waves are often referred to as guided waves, because the surfaces of the medium confine the waves to the geometry defined by the surface (3). Rayleigh waves propagate along the surface, confined to within a wavelength of the surface, while Lamb waves propagate in the interior of the plate, confined between the top and bottom surfaces. Lamb waves are popularly used in Structural Health Monitoring because they have a very low attenuation rate. *Fundamentals and Applications of Ultrasonic Waves* by Cheeke (3) lists the frequency range for guided wave applications as being  $10^5$  to  $10^6$  Hz for thin plates, rods, and shells.

The experiments described in this thesis all generate waves in thin aluminum plates in the guided wave frequency range. Rayleigh and Lamb wave modes are likely to

be present, so it is useful to know some of their unique characteristics. These characteristics are best understood in the context of their mathematical formulation. The following sections provide the problem statement, boundary conditions, and solutions for Rayleigh and Lamb waves. Table 1 lists material data used to calculate the waves speeds derived in the next sections.

**Table 1: Material values for 6000 series aluminum.**

Constant	Value
Poisson's ratio	0.33
Lamé constant $\lambda$	50.4 GPa
Lamé constant $\mu$ (Shear Modulus)	25.9 GPa
Elastic modulus	69 GPa
Density	2.7 g/cc
$C_1$ (transverse wave speed, or speed of sound for shear waves)	3097 m/s
$C_1$ (longitudinal wave speed, or speed of sound for pressure waves)	6153 m/s

The values for the Elastic modulus, density, and Poisson's ratio in Table 1 are an average of values taken from [www.matweb.com](http://www.matweb.com) (14) for 6000 series aluminum. All other values were calculated from formulas obtained in Cheeke's text: Fundamentals and Applications of Ultrasonic Waves (3).

### 2.1.1. Rayleigh waves

Rayleigh waves and Lamb waves have coupled longitudinal and shear components. I.A. Viktorov (15) gave a detailed description of the two-dimensional mathematical formulation for both Rayleigh and Lamb waves. Only a brief account of that description will be here. As shown in Figure 2, a plate is considered infinite in the direction of propagation,  $x$ . The plate has a finite thickness,  $2d$ , in the  $z$  direction.

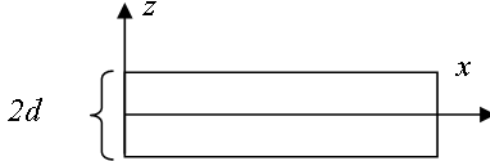


**Figure 2: Two-dimension plate with thickness 2d.**

The vector displacement of a particle,  $V$ , is written in terms of a scalar potential function,  $\varphi$ , and a vector potential function,  $\psi$ .

$$V = \text{grad } \varphi + \text{curl } \psi \quad 1$$

Equation 1 is from the Fundamental Theorem of Vector Analysis (16). Viktorov (15) then assumes that the wave is a plane wave thus the curl of the vector potential  $\psi$  is non-zero in the  $y$  direction only. This changes the vector potential to a scalar potential; denoted from this point on by  $\psi$ .

The potentials must satisfy wave equations in the longitudinal and transverse modes.

$$\begin{aligned} \frac{\partial^2 \varphi}{\partial x^2} + \frac{\partial^2 \varphi}{\partial z^2} + k_l^2 \varphi &= 0, \\ \frac{\partial^2 \psi}{\partial x^2} + \frac{\partial^2 \psi}{\partial z^2} + k_t^2 \psi &= 0 \end{aligned} \quad 2$$

Here,  $k_l$  and  $k_t$  are the wave numbers for the longitudinal and transverse bulk wave modes, respectively. Writing the displacements  $U$  and  $W$  in terms of the partial derivatives of the potentials leads to expressions for the stress components in terms of the potentials.

$$U = \frac{\partial \varphi}{\partial x} - \frac{\partial \psi}{\partial z}, \quad W = \frac{\partial \varphi}{\partial z} + \frac{\partial \psi}{\partial x} \quad 3$$



$$\begin{aligned}\sigma_{xx} &= \lambda \left( \frac{\partial^2 \varphi}{\partial x^2} + \frac{\partial^2 \varphi}{\partial z^2} \right) + 2\mu \left( \frac{\partial^2 \varphi}{\partial x^2} - \frac{\partial^2 \psi}{\partial x \partial z} \right), \\ \sigma_{zz} &= \lambda \left( \frac{\partial^2 \varphi}{\partial x^2} + \frac{\partial^2 \varphi}{\partial z^2} \right) + 2\mu \left( \frac{\partial^2 \varphi}{\partial z^2} + \frac{\partial^2 \psi}{\partial x \partial z} \right), \\ \sigma_{xz} &= \mu \left( 2 \frac{\partial^2 \varphi}{\partial x \partial z} + \frac{\partial^2 \psi}{\partial x^2} - \frac{\partial^2 \psi}{\partial z^2} \right)\end{aligned}\quad 4$$

To solve for the Rayleigh wave mode, one assumes the solution is a plane harmonic wave traveling in the x direction. The boundary conditions specify that  $\sigma_{zz}$  and  $\sigma_{xz}$  are zero on the top surface of the plate. The solutions for the scalar potentials in terms of the Rayleigh wave number k, longitudinal wave number  $k_l$ , transverse wave number  $k_t$ , frequency w, and an arbitrary constant A, are given in Equation 5.

$$\begin{aligned}\varphi &= -Ae^{i(kx-wt) - \left(\sqrt{k^2 - k_l^2}\right)z}, \\ \psi &= iA \frac{2k \left(\sqrt{k^2 - k_l^2}\right)}{2k^2 - k_t^2} e^{i(kx-wt) - \left(\sqrt{k^2 - k_l^2}\right)z}\end{aligned}\quad 5$$

The characteristic equation for finding k reduces to the following form given by Viktorov:

$$\begin{aligned}\eta^6 - 8\eta^4 + 8(3 - 2\xi^2)\eta^2 - 16(1 - \xi^2) &= 0 \quad 6 \\ \text{Where } \eta &= \left(\frac{k_t}{k}\right), \text{ and } \xi = \left(\frac{k_l}{k_t}\right)\end{aligned}$$

There is only one root, and it only depends on the value of Poisson's ratio ( $\nu$ ).

$$\eta_R = \frac{0.87 + 1.12\nu}{1 + \nu} \quad 7$$

For Poisson's value of 0.33 (aluminum), this value corresponds to a wave speed of 2987 m/s. This is about 93% of the transverse bulk wave speed.

### 2.1.2. Lamb waves

Starting with Equations 1 to 5, Lamb wave modes are found by setting the boundary conditions  $\sigma_{zz}$  and  $\sigma_{xz}$  to be zero at the top *and bottom surfaces* of the plate.

Then, the assumed solution takes the form given in Equation 8.

$$\begin{aligned}\varphi &= A \cos \sqrt{k^2 - k_t^2} z e^{ikx} + B \sin \sqrt{k^2 - k_t^2} z e^{ikx}, \\ \psi &= C \cos \sqrt{k^2 - k_t^2} z e^{ikx} + D \sin \sqrt{k^2 - k_t^2} z e^{ikx}\end{aligned}\quad 8$$

This leads to a pair of characteristic equations that determine the value of  $k$  given by Viktorov in the following dimensionless form.

$$\begin{aligned}\text{for symmetric modes} \quad \frac{\tan \sqrt{(1 - \zeta^2)} \bar{d}}{\tan \sqrt{(\xi^2 - \zeta^2)} \bar{d}} &= -\frac{4\zeta^2 \sqrt{(1 - \zeta^2)} \sqrt{(\xi^2 - \zeta^2)}}{(2\zeta^2 - 1)^2}, \\ \text{for anti - symmetric modes:} \quad \frac{\tan \sqrt{(1 - \zeta^2)} \bar{d}}{\tan \sqrt{(\xi^2 - \zeta^2)} \bar{d}} &= \frac{-(2\zeta^2 - 1)^2}{4\zeta^2 \sqrt{(1 - \zeta^2)} \sqrt{(\xi^2 - \zeta^2)}}\end{aligned}\quad 9$$

The following identities apply:  $\bar{d} = k_t d$ ,  $\zeta^2 = \frac{c_t^2}{c^2}$ , and  $\xi^2 = \frac{c_t^2}{c_1^2}$ . The values  $\xi$  and  $\zeta$  are given in terms of the Lamb wave phase speed  $c$ , the bulk transverse wave speed  $c_t$ , and the bulk longitudinal wave speed  $c_1$ . The first equation corresponds to modes that propagate in a symmetric fashion relative to the central axis in the  $x$  direction. The second equation corresponds to modes that propagate in an anti-symmetric fashion relative to the central axis in the  $x$  direction. Figure 3 shows exaggerated symmetric and anti-symmetric lamb wave modes propagating in a two-dimensional plate. For both mode shapes, motions in the longitudinal and transverse directions are coupled. In the literature, these modes are usually abbreviated with an ‘S’, for symmetric modes, or an ‘A’, for anti-symmetric modes, followed by the number of the mode.

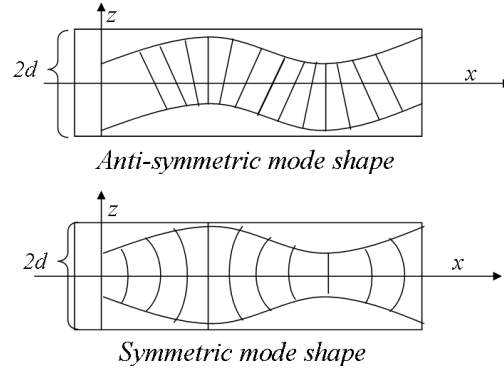


**Figure 3: Mode shapes for symmetric and anti-symmetric lamb waves.**

From these characteristic equations, the dispersion relations, a plot of the frequency thickness product  $\bar{d}$ , and the phase speed normalized to the bulk transverse phase speed ( $\frac{c}{c_t}$ ) can be generated. For any given value of  $\bar{d}$  only a certain number of symmetric and anti-symmetric modes, exist (13). Figure 4 shows the first and second symmetric (S0 and S1) and first and second anti-symmetric (A0 and A1) Lamb wave modes for aluminum. For a sufficiently thin plate, second order modes will only appear at higher frequencies. The first experiment described in this thesis never exceeded a frequency-thickness product of 1.67. Later experiments had geometry with varying thicknesses that resulted in frequency-thickness products up to 5.0.

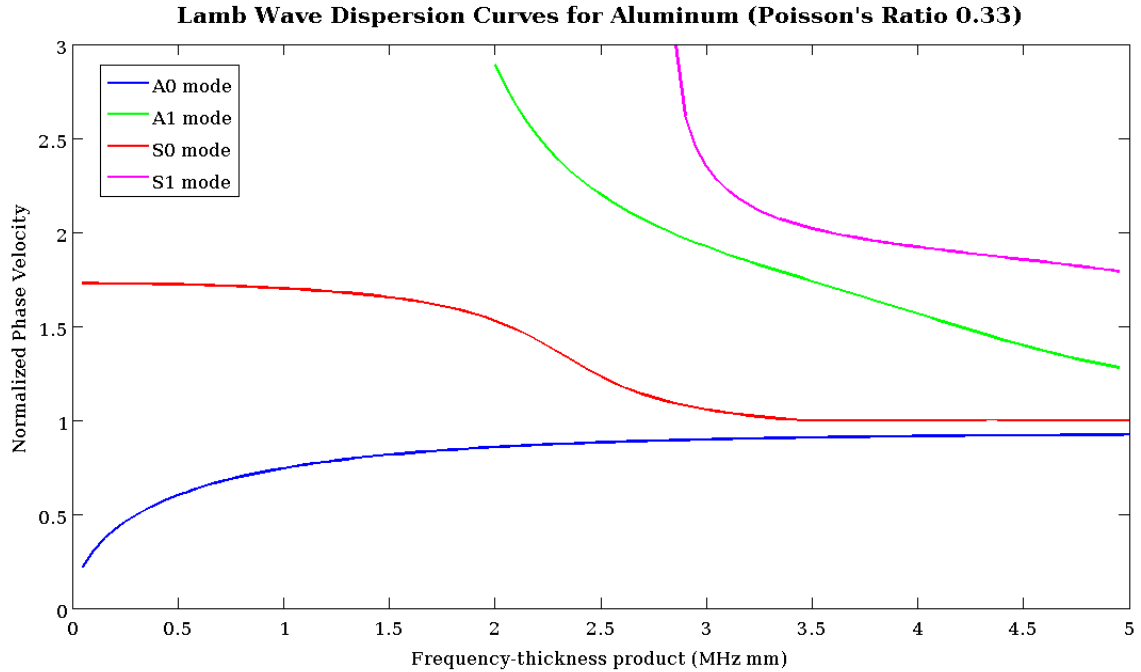


**Figure 4: Dispersion curves for the first and second symmetric and anti-symmetric Lamb wave modes. The data points for the plot were generated by code written in Mathematica™, which can be found in Appendix 1.**

## 2.2. Use of piezoelectric materials to excite and sense guided waves

Materials that exhibit the piezoelectric effect generate current under applied stress. Conversely, they generate strain (change shape) when exposed to an electric field (16). Piezoelectric materials are used extensively for ultrasonic transducers and stress sensors in a variety of shapes and sizes (17).

### 2.2.1. Method of excitation

The method used in the experiments described in this thesis uses periodic shearing perturbation of a finite region on the plate surface. A wafer made of piezoelectric material is bonded to the surface of a plate as shown in Figure 5. The piezoelectric materials are described as wafers in this case because they are much thinner than the thin

plates guided waves propagate in. The bottom surface of the piezoelectric wafer is grounded. Current is applied to the top surface of the piezoelectric wafer resulting in a change in voltage or electric potential. The change in voltage creates an electric field in the piezoelectric wafer causing the material to deform by the converse piezoelectric effect. Assuming the bond between the piezoelectric wafer and the plate beneath it is perfect, the deformation induced in the wafer results in elastic surface perturbations in the plate. If the change in voltage is oscillating, as it would be under an alternating current, the resulting elastic perturbations will also oscillate and form an elastic wave in the plate.

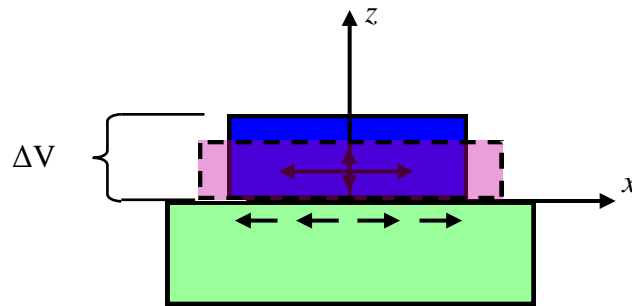


**Figure 5: A change in voltage across the piezoelectric wafer results in shearing perturbations that produce guided waves.**

This method of exciting elastic waves in plates produces all possible modes for a given frequency (15). Other methods exist that selectively excite specific modes, but are more cumbersome to use. The wedge method, for example, requires an ultrasonic beam to strike the surface at an angle. The angle must be carefully calibrated to get the desired results (15). This method, however, only requires a piezoelectric wafer bonded to the surface of the plate with two wire leads attached to it. The result is a very compact and lightweight transducer or sensor. However, producing all possible wave modes could be a drawback for ultrasonic testing techniques that use features of the signal that are wave mode-specific, such as wave speed.

Wave modes are usually identified in the signal by arrival times, or wave speed. However, if the distance from source to receiver is short, resolving Rayleigh and Lamb modes may not be possible. Viktorov describes a quasi-Rayleigh wave mode that exists near the source of perturbation. In this case, the first symmetric and anti-symmetric Lamb modes interfere and produce a wave that is a hybrid Lamb and Rayleigh wave mode. This wave moves between the top and bottom surfaces of the plate traveling at speeds somewhere between Rayleigh and Lamb mode speeds until the symmetric and anti-symmetric Lamb modes separate sufficiently. The equation used to estimate the distance required for the modes to separate by 180 degrees is given below from Viktorov's text. According to the text, Equation 10 is accurate to within 10%.

$$L = \left[ \frac{1}{4} + \frac{1}{8(1 - \eta_R^2)} + \frac{1}{8(1 - \eta_R^2 \xi^2)} - \frac{1}{2 - \eta_R^2} \right] e^{2k_R d \sqrt{1 - \eta_R^2}} \quad \mathbf{10}$$

From Section 2.1.1,  $\xi = \left( \frac{k_l}{k_t} \right) = \left( \frac{c_t}{c_l} \right) = \left( \frac{3097 \text{ m/s}}{6153 \text{ m/s}} \right) = 0.50333$  and  $\eta_R = 0.93203$ .

The quantity  $k_R d$  reduces to  $\frac{k_t d}{\eta_R}$ , where  $k_t d$  is the frequency-thickness product from the Lamb wave dispersion relations. For aluminum, the distance it takes for the modes to separate by 180 degrees (L) is 1.04 m at a frequency-thickness product of 1.0 MHz mm. Viktorov points out that any method used to produce Lamb waves by surface perturbations will also produce a quasi Rayleigh wave, so choosing a different excitation method would not have made a difference in this respect.

Despite these apparent complications to the signal, several researchers (Doyle et al. (7), Giurgiutiu and Cuc (18), Greve et al. (19), Nieuwenhuis (20), and Gomez-Ullate et al. (21)) have used piezoelectric wafers to excite and resolve Lamb wave in thin plates successfully. Most of these researchers were easily able to resolve the first symmetric

and anti-symmetric lamb wave modes at distances around 20 cm, at frequency-thickness products near or less than one MHz-mm. Viktorov briefly mentioned a dependence of Lamb mode amplitudes on the size of the transducer (15). In 2003, Giurgiutiu (22) went on to show that the dependence on amplitude with sensor dimensions could be exploited to select a preferred mode. Niewenhuis et al. (23) confirmed Dr. Giurgiutiu's work with a full multi-physics simulation. All of the experiments done for this thesis use transducer and plate dimensions similar to what was used in the research just described. In light of the findings from this research, it is likely that just one or two of the many possible modes dominate the signal. However, determining the modes from the signal in the time domain may be difficult, but not impossible. The distances between sensors in the experiments described in this thesis are approximately six cm. According to Equation 10, all of the signals used in the experiments in this thesis contain a quasi-Rayleigh wave mode.

### **2.2.2. Reception of guided waves**

Piezoelectric sensors are typically used in either a pitch-catch or a pulse-echo configuration (24). The pulse-echo configuration uses the same sensor to receive a signal as it does to send it. Usually, this configuration is used for reading the reflected portion of a transmitted wave. A pitch-catch configuration was used for all of the experiments in this thesis. This configuration uses two sensors, one for sending the wave and another for receiving it. The pitch-catch configuration was chosen for the experimental joint assessment method so that multiple interfaces in the joint could be assessed with the transmitted signal rather than the reflected signal.

The way guided waves are sensed by piezoelectric sensors is, generally, similar to the way the waves are created (3). Strain in the plate due to a passing wave is mechanically transferred to the piezoelectric material by the bond between the sensor and the plate. The piezoelectric effect converts the strain energy into electrical energy. An investigation into exactly how this process works with Lamb and Rayleigh waves was performed by Di Scalea et al. (25). They found that the response is dependent on sensor dimensions, frequency, and mode of wave incident to the sensor. The analytic model was found by solving for the voltage output in terms of the in plane strains and matching these strains with strains generated by the waves. This model was verified by experiment. They reported on a narrow band (tone burst) response and a broadband (harmonic) response. For the purposes of the research for this thesis, both narrow band and broadband are of interest. Di Scalea et al. reported that the narrow band response maxima were near the broadband for lower frequencies but diverged for higher frequencies. This suggests a difference in the way piezoelectric materials are able to detect Lamb and Rayleigh waves in both narrow and broadband signals. In addition, the corresponding maximum response was different for Lamb and Rayleigh wave modes.

### **2.3. Reflection and transmission of guided waves**

Reflection of guided waves by scattering off discontinuities in the medium is an important topic in Non-destructive Evaluation. Most Non-destructive evaluation techniques rely on some feature of a reflected wave (24). Wave scattering is a well understood phenomena, but the dispersive nature of Lamb waves creates a high degree of



complexity. If not complex enough, wave reflection and transmission at rough interfaces is complex for another reason.

### **2.3.1. Current research in wave scattering**

Reflection and transmission of guided waves occurs at any discontinuities in the medium. Changes in the wave, if detectable, have been used to find cracks (19),(26), changes in thickness (27), and changes in elastic properties due to applied load (7). Reflection and transmission coefficients are solved for specific modes, so different modes have to be identified in the received signal. This can be difficult with Lamb modes, as they can sometimes interfere and worse, they undergo mode conversion at interfaces that is highly dependent on frequency as shown in work done by Galan (28), Song et al. (6), and Morvan et al. (29). Complicated models of Lamb mode reflection at the free edge of a plate using a hybrid of boundary element and finite element methods have been tested with agreeable results in a couple of papers by Rose et al. (30), (27). Those models concentrated on the dependence of amplitude with frequency, so they were of particular interest to this research. Other researchers have formulated numeric models that highlighted other properties of Lamb waves. One by Lenoir and Duclos (31), in particular, highlighted the specific dependence of reflected Lamb modes on frequency by basing the model on phase derivatives, which use frequency as the dependent variable.

### **2.3.2. Wave interaction at poorly defined interfaces**

Wave interaction at an interface for normal incidence is normally formulated in terms of acoustic impedances of the materials that make up the interface. The reflection

(R) and transmission (T) coefficients of a perfect interface between two materials are given as the following (3):

$$T = \frac{2Z_2}{Z_1 + Z_2},$$

$$R = \frac{Z_2 - Z_1}{Z_1 + Z_2} \quad \mathbf{11}$$

The acoustic impedance is represented with the letter Z and a subscript for material one and material two. The incident wave is from material one, by convention.

If the material is the same on either side of the interface, the coefficients reduce to  $T = 1$  and  $R = 0$ . In this case, there is no reflection and the wave is completely transmitted across the interface. Situations involving an acoustic couplant or epoxy are often modeled with a layer of the couplant or epoxy between two areas of the same material. Following directly from Equation 11, the reflection coefficient is (3):

$$R = \frac{Z_{layer} - Z_1}{Z_{layer} + Z_1} \quad \mathbf{12}$$

If the layer is air and the surrounding material is aluminum, the reflection coefficient is calculated using values from Cheeke's text: Fundamentals and Applications of Ultrasonic Waves (3).

$$R = \frac{0.4286 - 17.33}{0.4286 + 17.33} = -0.95173 = 95\% \text{ reflection}$$

This means that only 5% of the wave energy is transmitted into the air layer. The same ratio applies at the air to aluminum interface leaving only 0.25% final energy transmission. This value is far lower than observed results (32) without taking into account the thickness of the air layer or the effect of a variable contact force. These other variables must be taken into account.

These formulas were developed for a well-defined interface between two materials. To be a well-defined interface, the interface must be perfectly in contact with both materials and have no net stress on the interface (3). A well-defined interface ensures that “continuity of normal and tangential components of stress and displacement (3)” can be used in the boundary conditions. This is necessary in order to use any of the mathematical tools developed for wave transmission across an interface. The easiest way to ensure the interface is well defined is to assume the interface is made of two perfectly flat surfaces. In reality, there is no such thing as a perfectly flat surface. When modeling a connection with an acoustic couplant, the couplant fills the tiny imperfections on the surface of each plate resulting in a couplant layer of varying thickness. Differences in thickness of the couplant layer do not come into the calculation, so the surfaces can be approximated to be flat. This approximation works especially well if the acoustic mismatch between the transmitting mediums and the couplant is not large. Then the dominate method of wave transmission is most likely the one given by the reflection and transmission coefficients of Equations 11 and 12. However, for a dry (no acoustic couplant or adhesive), roughly connecting surfaces, the model must be adjusted, as described in the next section.

#### **2.3.2.1. Spring interface model**

A popular model for dry or rough connections is to model the interface with a series of springs. Baik and Thompson (10) first showed the effectiveness of this kind of model with ultrasonic waves. Others (9), (11), (33) have since verified and made use of the spring interface model for ultrasonic or guided waves. Statistical approaches (34),

(35) and rheological models have also been studied (36), (37), (38), (39). For the spring models, the interface is conceptualized as a series of cracks or small inclusions. The stiffness of the interface is related to the size of the inclusions and the density of the medium filling the inclusions (33). This model creates fully specified boundary conditions by ensuring continuity of stresses across the boundary. It also creates conditions that are dependent on properties of the boundary, which is useful conceptually. Spring models have been shown to work well with rough interfaces between different media as well (40). Researchers in the field of acoustics model similar structures at larger length scales than the ultrasonic length scale, like the air gap between panels used for soundproofing, as a spring (41).

The quasi-static reflection and transmission coefficients for a single material, as reported by Baik and Thompson in 1984, are:

$$R = \frac{j\omega(Z/2\kappa - m/2Z)}{(1 - m\omega^2/4\kappa) + j\omega(Z/2\kappa + m/2Z)} \quad \text{and}$$

$$T = \frac{(1 + m\omega^2/4\kappa)}{(1 - m\omega^2/4\kappa) + j\omega(Z/2\kappa + m/2Z)} . \quad 13$$

Here,  $j$  is the mode number,  $m$  is the mass per unit area,  $\omega$  is the angular frequency of the incident wave,  $Z$  is the acoustic impedance of the material, and  $\kappa$  is the interfacial stiffness defined as stress (applied in tension) and the local deformation near the interface due to cracks or pores. Figure 6 shows  $\kappa$  in terms of the additional stretch due to applied stress.

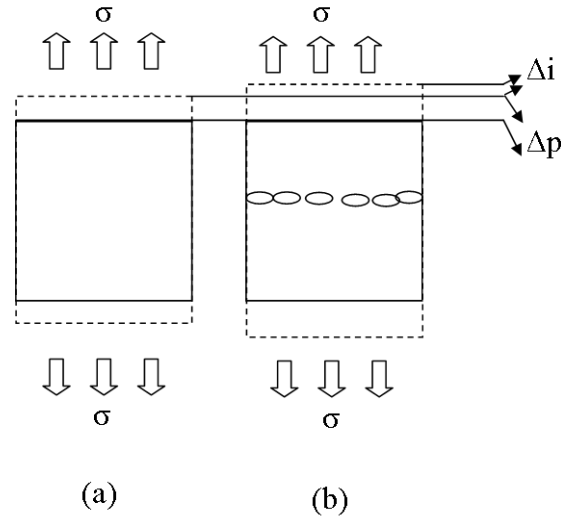


**Figure 6: Definition of interfacial stiffness from Baik and Thompson.** Side a shows a material under stress elongating by an amount  $\Delta p$  under stress  $\sigma$ . Side b shows the same material under the same stress with the addition of inclusions (depicted by small ovals). This material elongates by  $(p + \Delta i)$ . Interfacial stiffness,  $\kappa$ , is then given by  $\sigma / \Delta i$ .

These approximate values for R and T are highly dependent on frequency, which has been verified by all the researchers mentioned in this section—including Xin, Lu, and Chen (41) with their work on double panel partitions. According to this model, the reflection and transmission of ultrasonic waves is dependent on the material properties, the frequency of the incident wave, and the roughness of the interface.

#### 2.4. Current research into ultrasonic inspection of rough interfaces and joints

The previous sections discussed physical phenomena related to excitation and reception of guided waves. The following discussion relates to research that utilizes that physical phenomena in different ways to inspect rough interfaces and joints in aerospace structures. The research found in the literature concerning rough interfaces is generally

not in the field of aerospace inspection. For this reason, it is presented in a separate section. For each section, information is presented in order of increasing complexity.

#### **2.4.1. Rough interfaces**

The frequency range used in the following studies is much higher than the range used in the experiments described in this thesis. The reason is often that the researchers are focused on finding small cracks in the panel that have closed due to external compressive forces. However, many of the concepts still apply to the research presented in this thesis.

As mentioned in the introduction, Dryer-Joyce et al. (9) used ultrasound to investigate a roughly contacting interface in the context of detecting cracks. They were able to show a correlation between contact stiffness and the reflection coefficient two to three orders of magnitude more sensitive than by using load deflection measurements. These findings are of particular importance to this thesis, as this demonstrates a direct correlation between the reflection of waves (and thus transmission) and the contact pressure at the interface. The same researchers went on to extend this principle to machined parts. They were able to show good agreement between an analytic model and experiments. The model is easy to follow conceptually, using the Baik and Thompson quasi-static boundary conditions and principles of Hertzian contact. Hertzian contact is the classic problem involving elastic deformation of solids due to external pressure that leads to an increased surface area (42). By this model, increased pressure leads to increased surface area. Increased surface area implies that wave transmission would increase.

Liaptsis et al. (43) showed empirical data correlating contact pressure and the reflection of ultrasonic waves could be used to determine the contact pressure at an interface. He used the same data to validate the quasi-static spring model for ultrasonic frequencies lower than 4 MHz.

In 1995, Pecorati et al. (34) published a two-part study on ultrasonic waves reflecting off rough surfaces. They found that the quasi-static boundary conditions given by Baik and Thomson (10) could be extended from flat imperfect boundaries to imperfect boundaries with irregular profiles. They were able to do this by considering the stiffness in the tangential and normal directions separately. This implies that the frequency dependent spring interface model is still valid even if the connecting surfaces are very rough or are warped, so the same transmission or reflection behavior can be expected even in extreme cases.

Together, the work of Dryer-Joyce et al. and Liaptsis et al. give good evidence for the utility of inspection of rough surfaces by studying the reflected amplitudes of ultrasonic waves. In light of this work, the reflection and transmission of ultrasonic waves across a rough interface is dependent on the material properties, the frequency of the incident wave, the roughness of the interface, and the applied stress to the interface. According to Pecorati et al., this behavior should persist even in more extreme cases of roughness.

#### **2.4.2. Joint inspection in aerospace structures**

A lot of the ultrasonic inspection research done specifically for aerospace structures is done using lap joints. These investigations, like the rough surface

investigations above, usually concentrate on a simple geometry with one interface or one feature that causes scattering. Song et al. (6) did a study on the reflection of the A0 (first anti-symmetric) Lamb wave mode on a lap joint. The joint in this experiment was machined from a single piece of steel, and therefore it did not contain an interface. Despite this simple geometry, many important things were learned from the reading of this paper. The numeric model used in this paper was a hybrid boundary element and finite element program that simulated the scattering of a single Lamb wave mode. Complicated mode conversion phenomena was predicted in the simulation and observed experimentally. In addition to mode conversion, the transmission amplitudes were highly dependent on frequency and plate dimensions. This complexity exists despite the absence of a rough connection or other wave modes.

Stepping up the complexity, several researchers have done similar studies with joints that contain adhesive. A perfectly bonded adhesive joint has well defined boundaries. However, it can be tricky to tell if changes in the signal are due to break down of these boundaries or some other type of damage (like creep in the adhesive). Puthillah et al. (5) addressed several different types of damage to adhesively bonded lap joints. Challis et al. (4) used an intelligent signal processing in the form of an artificial neural network to process the data.

Ultrasonic investigations of bolted structures must also consider scattering due to the presence of the bolt itself. Miller et al. (44) did an analysis of scattering in a plate due to a single bolt. They found that the scattering amplitudes decrease as the bolt moves out of the plate, suggesting that applied torque appears to increase damping in the signal. They also presented evidence that an effective domain exists for detecting loose bolts.



Signals traveling in regions farther from the bolt are not affected by it. Doyle, Zagrai, Arritt, and Çakan (7) found that signals in the presence of a bolt with pre-load have a phase shift. This effect was exploited to examine plates without having to deal with properties of reflected waves and the necessary boundary conditions. Lovell and Pines (8) did a study focusing on the nonlinear joint dynamics of bolted single lap joint. Loss of preload in the bolt was correlated with an ultrasonic scattering matrix. From this information, they were able to find an effective joint stiffness.

Francoeur et al. (45) dealt with the increasing complexity of the problem with a system that estimated unknown parameters. The method was able to show the progression of damage with the use of a baseline. In this case, roughness in the interface was not considered. The highest level of complexity involves taking the rest of the structure into account. Champaney et al. (46) proposes using a multi-analysis computation strategy for solving contact problems in the context of the larger aerospace structure.

## **2.5. Summary**

The method used to produce guided waves for the purpose of joint inspection was chosen because it is compact and lightweight. However, the signal it produces is a complicated mix of guided wave modes that cannot reasonably be resolved into separate modes at close distances. Therefore, testing techniques that involve mode-specific features are not practical.

Reflection or transmission amplitudes are not mode-specific features. However, reflection and transmission amplitudes are dependent on several variables. Scattering of

guided waves occurs at any discontinuities in the medium. They also undergo mode conversion at interfaces that is highly dependent on the frequency of the incident wave.

According to spring interface model, the reflection and transmission of ultrasonic waves is dependent on the material properties, the frequency of the incident wave, and the roughness of the interface (even if that interface is very rough). Additional research has shown that reflected amplitudes are also a function of the applied stress to the interface. This means that, knowing the basic material properties and the frequency of the incident wave, the amplitude of the reflected wave could be used to gauge roughness or applied stress to the interface.

In an actual joint, scattering could take place off bolts as well as changes in thickness and dry connections. This increases the complexity of the problem. Research suggests a difference in the way piezoelectric materials are able to detect Lamb and Rayleigh waves in both narrow and broadband signals. The testing method would need to consider this possibility. Use of a baseline may help eliminate some of these extra variables.

## CHAPTER 3: PROOF OF CONCEPT EXPERIMENT

This is the first of three experiments conducted for this thesis. All tests described in this chapter were conducted at the University of New Mexico. The intent and goals of this experiment are basic in scope. The lessons learned in this experiment were applied to later tests.

### 3.1. Intent and goals of the experiment

This experiment was intended to simulate a very simple panel-to-panel connection in a satellite. The first goal was to show that wave energy could be transmitted and received by piezoelectric sensors across a rough, dry connection. Once that was achieved, the second goal was to correlate changes in joint rigidity with transmitted wave energy. From the literature review and by initial investigation, wave amplitudes were known to be frequency dependent. Therefore, a range of frequencies was considered. To simplify the data set, a single parameter based on transmitted wave energy was devised.

### 3.2. Sample joint

A simplified version of a panel-to-panel connection in a satellite was made using two Aluminum (Al 3003) plates, 15.2 cm x 15.2 cm x 0.165 cm, joined by two 90 degree, 2.5 cm zinc-plated steel brackets, as shown in Figure 7. The brackets were bolted at the edges of the plates, leaving the center section of the joint free of support. This was done to minimize wave reflections from the bolts. Pan-head, slotted, machine screws (M6-1.00 x 30) were used with hex nuts to bolt the brackets to the aluminum plate. No

attempt was made to smooth or sand the plate edges after the plates were cut, and no glue or any kind of acoustic couplant was applied to the joint.

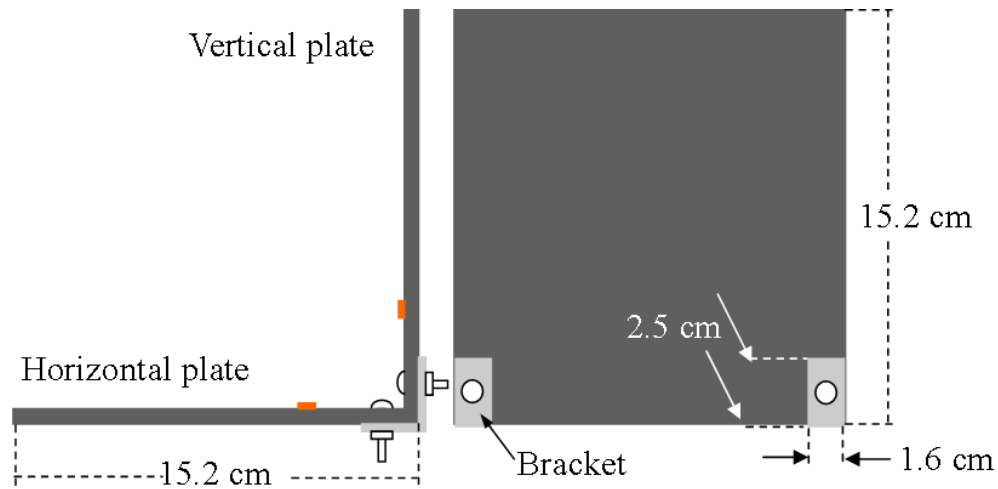


**Figure 7: Back and side view of the sample joint showing size of plates and placement of brackets.**

### 3.3. Sensors

Four piezoceramic sensors (PiezoSystems Woburn, MA, model: PSI-5A4E) were used in this experiment. They were each 8 mm by 8 mm by 2 mm, custom-cut from the same sheet of material by the manufacturer. Electrical and Mechanical properties of these sensors can be found in Appendix 2.

#### 3.3.1. Placement of the sensors

The four piezoceramic sensors were placed on the joint as shown in Figure 8. The piezoceramic plates attached to the vertical aluminum plate were designated V1 and V2. Likewise, the piezoceramic sensors attached to the horizontal aluminum plate were designated H1 and H2. All tests were conducted between pairs of sensors located across

the joint from one another. From this point, all references to a sensor pair are formatted with the transducer first receiving sensor second. (Example: V1 H1.)

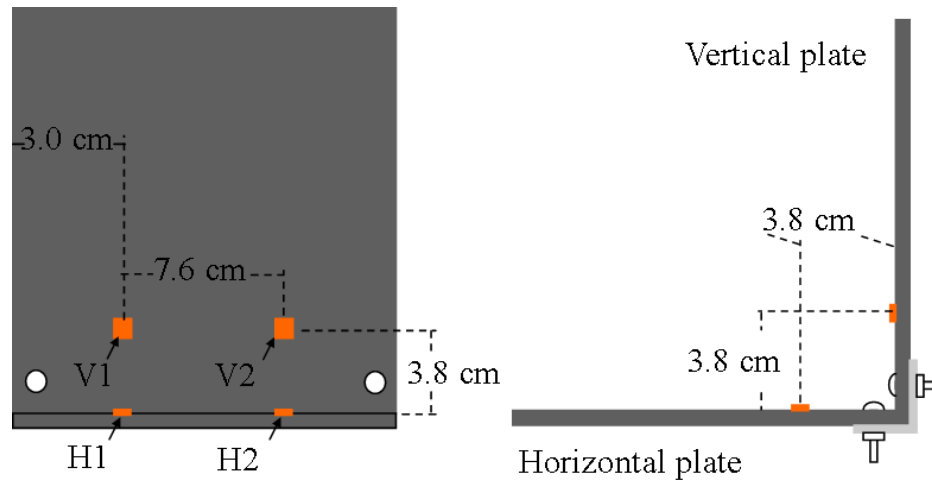


**Figure 8: Front and side view of the sample joint showing the placement of the sensors.**

Figure 9 shows the bonding and wiring method used on the piezoelectric sensors. The bottom of each piezoceramic sensor was bonded to the surface of the aluminum plate with conductive epoxy. A 20 AWG solid copper wire was soldered to copper foil, then bonded to the top of the piezoceramic plates with the same conductive epoxy. Each aluminum plate was connected to ground using the ground wire leads connected to the National Instruments PXI system. The PXI system, explained in more detail in a later section, was the equipment used to create and acquire high frequency voltage signals.

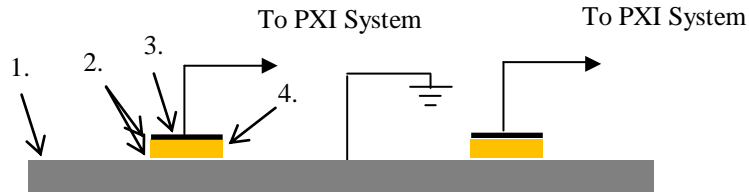


**Figure 9: Bonding of the sensors to the plate**

- 1. 15.2 cm by 15.2 cm. 3003 aluminum plate, 1.65 mm thick.**
- 2. CircuitWorks® Conductive Epoxy.**
- 3. 0.15 mm thick copper foil.**
- 4. 8 by 8 mm piezoceramic plate with PiezoSystems' Designation PSI-5A4E, 2 mm thick.**

### **3.3.2. Dynamic behavior and resonance of piezoelectric sensors**

The behavior of a piezoelectric element is categorized into two groups: static to near static behavior and dynamic behavior. Static to near static behavior is characterized as having an input frequency far below resonance. Dynamic behavior is characterized as having an input frequency higher than the natural resonance frequency of the crystal (47). A wide range of frequencies was used for this experiment, so dynamic behavior in the sensors was expected.

With dynamic behavior, the crystal is in a state of forced vibration. Like most forced vibration systems, the piezoceramic plate will resonate at the input frequency but most readily near its natural frequencies and their overtones (16). The natural frequencies and overtones of a rectangular parallelepiped may be found by the following approximate relationship provided in the text: Piezoelectricity; an introduction to the theory and applications of electromechanical phenomena in crystals by Walter Cady.

(16):

$$f_h \approx \frac{h}{2L} \sqrt{\frac{q}{\rho}}$$

14

The factor  $h$  is the order of the overtone,  $L$  is the length in the direction of wave propagation,  $\rho$  is the density, and  $q$  is the effective stiffness factor. The factor  $q$  may be approximated by using Young's modulus (16).

### 3.3.2.1. Estimation of the natural frequency

The following values were calculated from Equation 14 for the piezoceramic materials used in the proof of concept experiment that is described in the next chapter. Values for Young's modulus and density were obtained from the manufacturer (see Appendix 2):

For an 8 x 8 x 2 mm piezoelectric ceramic used in the experiment, the first resonance frequency in the 1-1 direction (and the 2-2 direction) was calculated to be 181.805 kHz.

$$\frac{1}{2 (0.008 \text{ m})} \sqrt{\frac{6.6 \times 10^{10} \text{ N/m}^2}{7800 \text{ kg/m}^3}} = 181805 \text{ Hz}$$

The first overtone for the 1-1 direction should be around 363.609 kHz.

$$\frac{2}{2 (0.008 \text{ m})} \sqrt{\frac{6.6 \times 10^{10} \text{ N/m}^2}{7800 \text{ kg/m}^3}} = 363609 \text{ Hz}$$

The first resonance frequency for the 3-3, or thickness, direction was calculated to be 645.497 kHz.

$$\frac{1}{2 (0.002 \text{ m})} \sqrt{\frac{5.2 \times 10^{10} \text{ N/m}^2}{7800 \text{ kg/m}^3}} = 645497 \text{ Hz}$$

These numbers are about 50 kHz lower than the location of the maximum peaks observed in the experimental data (shown in the results section). This is somewhat expected as using Young's modulus for  $q$  ( $q$  is a slightly larger number) should make the approximation lower than observed values. There should also be some difference due to the copper loading on the top of the piezoelectric plate and to imperfect glue bonding with the aluminum sample. According to Cady (16), the accuracy of Equation 14 further degrades at the overtones.

### **3.4. Mechanical assessment of joint rigidity**

A quantifiable mechanical assessment of the joint rigidity was needed to make a valid comparison with the energy transmission amplitudes obtained in the experiment. For this geometry, the contact force produced by the bolts is not in line with the contact the plates make with each other. However, the torque applied to the connecting bolts between the vertical plate and the bracket affect the rigidity of the joint. When the bolts are loosened, the decrease in contact between the bracket and the plate will result in increased movement inside the joint, making the joint loose. At the same time, the alignment of the plates with respect to one another can change. While reducing tension in the bolts should make the joint loose, possible shifting of the plates can either decrease or increase connectivity in the joint. Therefore, bolt tension alone is not an accurate measure of the joint rigidity, so a more direct measurement of the joint quality was chosen.



### 3.4.1. Characterization of the joint between two extreme cases

This method of joint characterization first idealizes the model joint as a thin beam with one end attached to a support and the other end free. The free end is subject to a load perpendicular to the beam as shown in Figure 10.

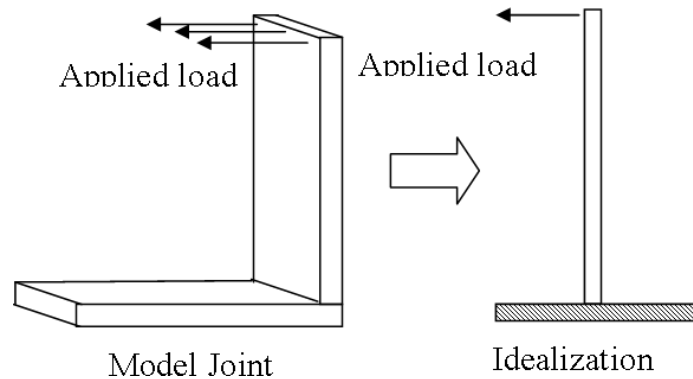


**Figure 10: Idealization of model joint.**

If the supported end of the beam in the idealization of the joint is pinned, or has no resistance to rotation, then the beam will undergo rigid body rotation under any load, as shown in Figure 11.

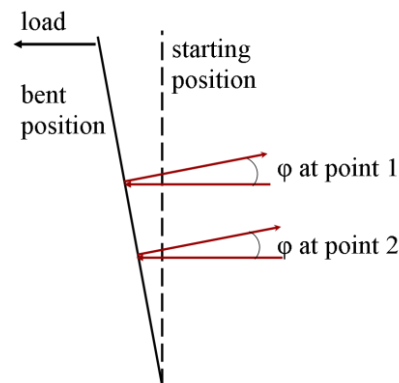


**Figure 11: A beam with one end pinned will have the same rotation value at point 1 and point 2.**

The rotation away from the original vertical position,  $\phi$ , at any point will be the same. Therefore, the ratio of  $\phi$  between any two points will always be one.

If the supported end of the beam is fixed, as shown in Figure 12, then no rotation at the joint is allowed and the beam will bend under load. Euler-Bernoulli bending can be used to describe the bending of the beam.

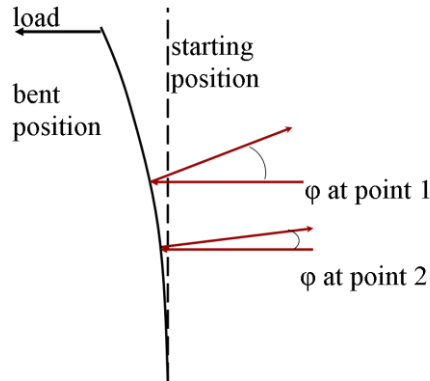


**Figure 12: A beam with one end fixed will bend. The rotation values for point 1 and point 2 will be different.**

With the load applied at the top of the plate, the rotation ( $\phi$ ) at a point is given by the following well-known relationship for a cantilever beam (48):

$$\phi = \frac{P}{2EI}(x^2 - 2Lx) \quad 15$$

P is the load, E is the Modulus of Elasticity, I is the second moment of area about the axis perpendicular to the bending motion, L is the length of the plate in the direction of bending, and x is the distance from the fixed joint to the point in the direction of bending. The angle of rotation,  $\phi$ , is the angle the tangent makes with the unbent position. The ratio of  $\phi$  for the actual model joint will fall between two extremes: 1.0 is the lower bound and the upper bound is given by Equation 16.

$$\text{upper bound} = \frac{\varphi_{\text{point 1}}}{\varphi_{\text{point 2}}} = \frac{(x_{\text{point 1}}^2 - 2Lx_{\text{point 1}})}{(x_{\text{point 2}}^2 - 2Lx_{\text{point 2}})} \quad 16$$

The actual joint is supported only at the edges by two brackets. The boundary conditions are not the same all the way across the joint. To minimize deflections that were not accounted for by the idealized model, measurements were only taken on the vertical line in the center of the vertical plate, directly under the applied load. The support at the joint is also much closer to a pinned condition than to the fixed condition. It is not expected that any measurements made on the model joint will be close to the upper bound.

### 3.4.2. Deflection measurement set-up

The entire model joint was attached to a heavy steel plate by securing the horizontal plate to elevated steel supports as shown schematically in Figure 13. This was done to minimize deflections in the horizontal plate and to counter the applied load.

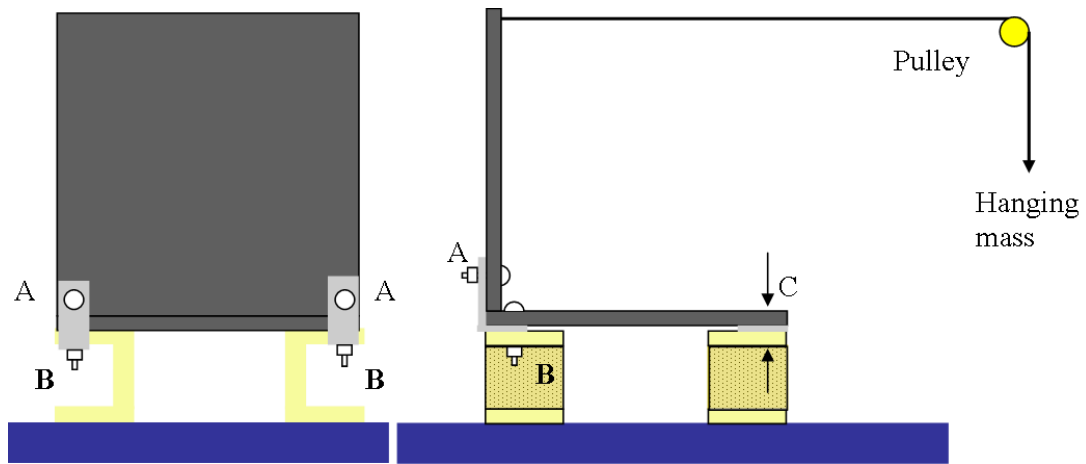
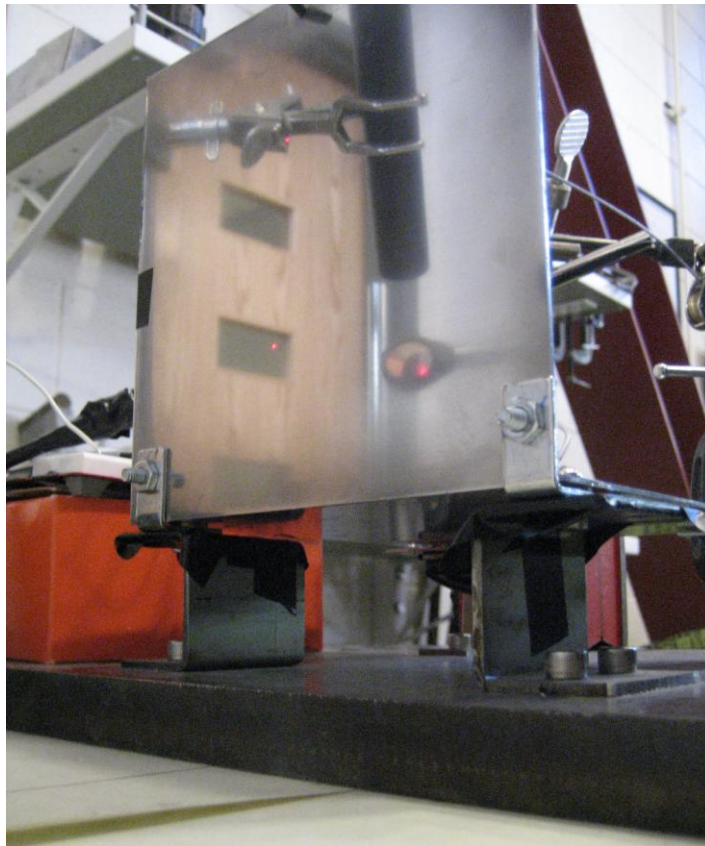


Figure 13: Back and Side view of joint attached to a steel plate.

A 1.6 mm diameter steel cable was attached to the vertical plate and a strung over a pulley. In Figure 13, the bolts at location A were periodically adjusted, bolts at location B were tightened and left alone, and one inch C-clamps were used to secure the far edge of the horizontal plate. A flat piece of steel that was the same thickness as the angled bracket making the joint was inserted between the support and the horizontal plate at the far end from the joint in order to ensure the horizontal plate was level.

Deflections in the vertical plate, with respect to the horizontal plate, were made by observing changes in a laser beam reflected off the back of the vertical plate. Special polishing paper of increasingly high grit (up to 3000 grit) was used to wet sand the back of the vertical plate to a high shine to reflect a low level-laser beam as seen in Figure 14.



**Figure 14: Photograph of the back view of the test subject secured to a heavy steel plate. The back of the vertical plate was polished to reflect a low-level laser beam.**

The entire apparatus was situated on a workbench. The horizontal plate was leveled so that it sat in the plane of the workbench. This was done so that the vertical plate could be rotated in reference to the horizontal plate and all subsequent measurements could be made in reference to the plane of the workbench. Figure 15 shows a top down view of the test setup.

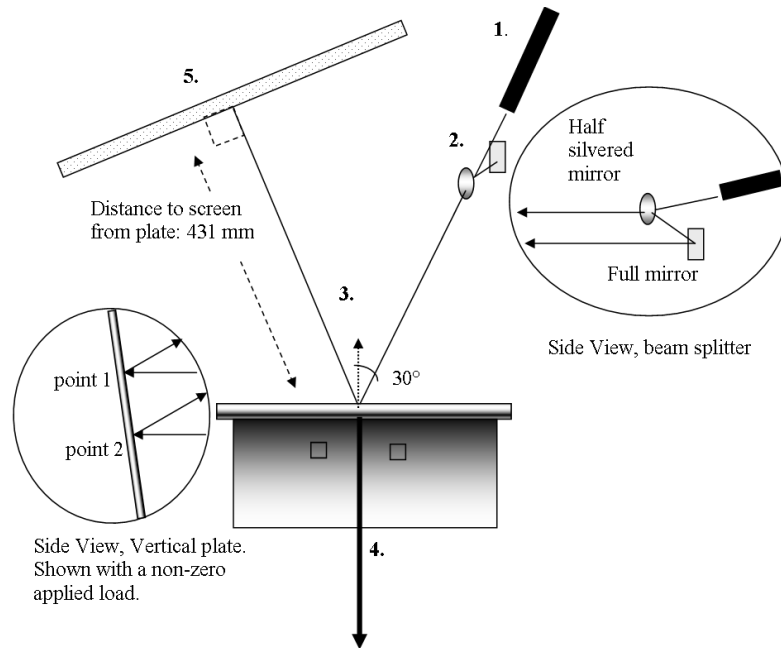


**Figure 15: Top down view of the experiment.**

- 1) Source: A class 3a, 5mW red laser beam.**
- 2) The beam is split into two beams, both parallel to the workbench.**
- 3) The beams strike the plate at 30 degrees to the normal of the plate in the horizontal plane at point 1 and point 2. The beams reflect at  $-30$  degrees from the normal toward the screen.**
- 4) Applied force causes the plate to pivot about the joint. The initial load is zero; the vertical plate makes a right angle with the workbench.**
- 5) The screen makes a right angle with both beams. The initial location of the beams (with zero applied load) is recorded as the origin. As the plate is deflected, the beams change position on the screen.**

All measurements and leveling of the beam were done by hand. The workbench used was covered with paper so that the angles and positions for the test setup could be measured with a ruler and protractor. Two-millimeter graph paper attached to a sheet of foam core was used for the screen. The laser beam was a common laser pointer. The beam was leveled by comparing the vertical distance on a screen placed at several horizontal distances up to 2.7 m. A level and square were used to ensure the screen was perpendicular to the floor and the workbench was level with the floor. To reduce the beam size, an opaque white label sticker with a pinhole in it attached to the end of the pointer. The spread in the laser beam was tested at various distances. At 2.7 m, there was no visible beam spread. However, the polished surface of the aluminum plate was not perfect, and the reflected beam spread to 1 mm in diameter at a screen distance of 4.31 cm from the vertical plate. This was acceptable because the 2 mm grid on the screen determined the smallest increment that could be measured.

### **3.4.3. Deflection measurement procedure**

The force described in Figure 15 was applied using a 1.6 mm diameter steel cable attached to the top of the vertical plate and extended over a pulley. This cable was used to suspend a known mass over the floor, thereby applying a horizontal load to the vertical plate. For the test, mass was added to a platform attached to the cable in increasing amounts of about 100g.

After the initial positions of both beams on the screen were recorded, load was added in approximately 100g increments. Each change in mass bent the vertical plate, and the reflected beam changed position on the screen. This change was recorded as  $\Delta x$

for the horizontal direction and  $\Delta y$  for the vertical direction. The geometric relationship between  $\Delta x$ ,  $\Delta y$ , and  $\varphi$  was derived by considering the motion of the plate in the vertical plane and the horizontal plane separately. The derivation of the following equations is included in Appendix 3.

$$\varphi = \frac{1}{2} \tan^{-1} \frac{\Delta y}{431 + \Delta x} \quad 17$$

$$\text{Joint Rigidity Ratio} = \frac{\varphi_{point\ 1}}{\varphi_{point\ 2}} \quad 18$$

### 3.5. Measurement of wave energy transmission

Most of the tests were conducted in the span of a few days to try to limit changes in temperature and humidity from affecting the test results. Once the bolts were adjusted, friction on the bolt threads, friction in the joint itself, and plasticity effects from over-tightening the bolts made each adjustment unique. The laser that was used to measure the deflection was kept on to monitor the position of the plate during all tests.

#### 3.5.1. Equipment and LabView™ programming

Signals were generated and received with a National Instruments PXI system. The system included LabView 8.5 (and later 8.6) which was run on a Dell SPS M1330 laptop, a PXI 1033 chassis, PXI 5102 High-Speed Digitizer, and a PXI 5402 Signal Generator. The signal generator has a maximum output voltage of +/- 5 V and a maximum sample rate of 400 MS/s for the type of function generated in these experiments. Neither of these limits was exceeded. The digitizer has a maximum sample rate of 20MS/s, which was the rate used to collect all data.

Virtual Instrument (vi) programs written in LabView 8.5 (and later 8.6) controlled the equipment and wrote the collected data to a text file for later analysis. The programs automated the data collection process so that input by the user was only needed when sensors or variables relating to the test subject needed adjustment or change. Documentation for these programs is located in the appendix.

### **3.5.2. Procedure**

The function generator induced a single tone at a constant excitation voltage at a transducer for 0.01 seconds. While the function generator was running, the amplitude of the output wave at a sensor, located across the joint from the transducer, was recorded with the digitizer. A virtual instrument program (vi) was written as a sub-routine to automatically collect a series of these single tone measurements for a range of frequencies from 100 kHz to 1000 kHz in 1.0 kHz increments. The master program used this sub-routine to automate the data collection for input voltages of 1.0, 2.0, and 3.0 volts with three trials each and store the data in a text file for later analysis. Each measurement made with this program resulted in nine files of data. Appendix 3 contains diagrams of these programs.

With the vertical plate under zero load, measurements were performed with each of the four piezoceramic wafers acting alternately as sensor and transducer. The entire procedure was repeated after each bolt adjustment and subsequent rigidity characterization by the mechanical assessment method described previously.



Noise levels were recorded for each sensor on each day of testing. This was done by running the experiment with no transducer connected. For all days tested, the average noise level recorded for all four sensors was 0.03 volts.

### 3.5.3. Calculation of energy parameter $E_j$

A plot of the raw data from each frequency sweep measurement shows voltage on the ordinate and frequency in kHz on the abscissa is shown in Figure 16.

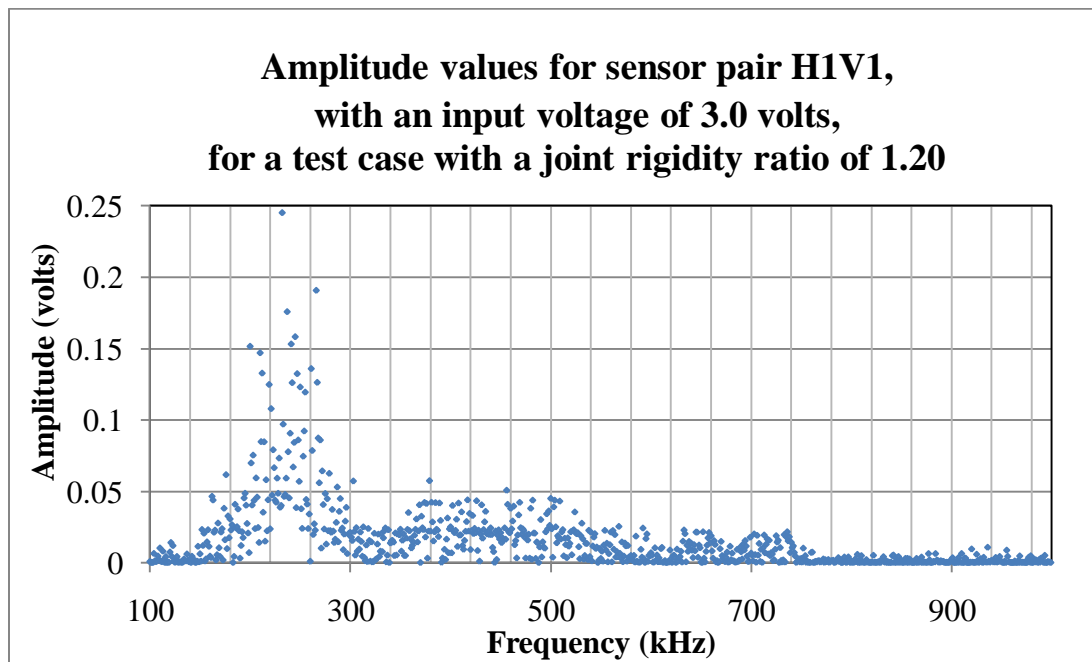


**Figure 16: Raw data collected at sensor pair H1V1 with an excitation voltage of 3.0 volts. The large peak near 220 kHz corresponds to the resonance frequency of the piezoceramic sensor.**

Each voltage value corresponds to a maximum output reading for a wave sent at the specific frequency listed on the plot. The largest peaks correspond to the resonance characteristics of the piezoceramic sensors used to excite and sense the signal. The

transducer will send a stronger signal at resonance and the sensor will be more sensitive at resonance. Although the piezoceramic wafers used were the same material and cut to very close to the same size, differences in the solder joints and bonds to the aluminum affect the resonance frequency. Consequently, the results obtained from a specific pairing of sensors will be different from other pairings. An estimation of the resonance frequency for the piezoelectric wafers used was given in Section 3.3.2.1. Estimation of the natural frequency. This value was 182 kHz, which was explained to be a low estimate.

The data collected is not a Fourier Transform of a single signal. It is a collection of largest amplitudes for multiple signals sent at a range of frequencies. In addition, each signal was altered by passing through the joint. Never the less, the raw data was analyzed using the same methods that are commonly used to analyze a single signal in the frequency domain. First, the amplitude values were normalized to the excitation voltage and then squared to transform the data so that a Power Spectral Density plot could be made. The energy contained in the largest peak was obtained by integrating from 200 to 300 kHz. A trapezoidal rule was used to do the integration on the discrete data set. The resulting value was divided by the bandwidth (assumed to be 1 kHz) to result in units of normalized amplitude<sup>2</sup>, a value proportional to the energy in the signal. The resulting energy parameter,  $E_j$ , characterizes the energy transmitted across the joint in a single value. Normalization ensures that perfect transmission at all frequencies between 200 and 300 kHz would give an  $E_j$  value of 1.0; a value of zero would indicate no transmission. The process is summarized in Equation 19.

$$E_j = \frac{\int_{200 [kHz]}^{300 [kHz]} \left( \text{amplitude [volts]} * \frac{1}{\text{excitation voltage [volts]}} \right)^2 df}{1 [kHz]} \quad 19$$

### 3.6. Results and analysis

Programs written in LabView were used to calculate all  $E_j$  values reported in this section. Documentation for these programs is contained in Appendix 3.

#### 3.6.1. Results of the mechanical joint assessment

The two points on the vertical plate chosen to be points of interest measured 106 mm and 62 mm, respectively, from the joint. Using these values for  $x_{\text{point1}}$  and  $x_{\text{point2}}$  in Equation 16, the upper bound is 1.4. Therefore, the ratio of the values measured at 62 mm and 106 mm should fall between 1.0 and 1.4, with the larger values representing test cases with a more rigid joint than the lower values.

At each mass increment, the rotation values,  $\phi_{106 \text{ mm}}$  and  $\phi_{62 \text{ mm}}$ , were calculated from the corresponding change in location of the reflected laser beam on the screen by Equation 17. The error associated with the deflection measurement is +/- 2.0 mm in both the x and y directions. The ratio of the rotation values (Equation 18) at 16 different mass increments (starting at about 0.9 N and ending at 14.7 N) for each joint rigidity case tested was tabulated. Of these, only the last 13 values were averaged. The first three data points were determined to be less reliable because the method used to detect curvature in the plate was not sensitive enough to detect the small changes in curvature that resulted at these lower loads. Two of the test cases have overlapping intervals, because the measured joint quality of these cases was very close. They were included in the correlation test as points of interest. The resulting values for the five test cases presented

have a 95% confidence level for each at about +/- 0.01. The values and confidence intervals are presented in Table 2.

**Table 2: Mechanical assessment of the joint after the bolts joining the brackets to the vertical plate were adjusted five times. The joint rigidity ratio and confidence levels are reported.**

Test number	Joint rigidity ratio	95 % Confidence level	Confidence interval, lower bound	Confidence interval, upper bound
1	1.20	0.01065	1.19	1.21
2	1.08	0.01404	1.06	1.09
3	1.14	0.00709	1.14	1.15
4	1.19	0.01195	1.18	1.21
5	1.24	0.01185	1.23	1.25

### 3.6.2. Linearity of the system

The tests were conducted at excitation voltages of 1.0, 2.0, and 3.0 volts. This was done to test the linearity of the system to the excitation voltage. If  $E_j$  is linear with respect to the excitation voltage, then  $E_j$  values obtained from different excitation voltages would be the same. If not, then raw data from different excitation voltages could not be normalized as described in Equation 19 and compared. It is possible that energy lost or gained from reflections in the panel or lost converting electrical energy to and from mechanical energy in the piezoceramic, sensors could have some non-linear influence on the transmission amplitude. Linearity was expected, but checking was necessary. For each test case and each sensor pairing, the output energy for each trial was found. Output energy was found with a process similar to finding  $E_j$ , as given by the following equation.

$$E_{trial \#} = \frac{\int_{200 [kHz]}^{300 [kHz]} (amplitude [volts])^2 df}{1[kHz]} \quad 20$$

The final value of the output energy was the median of these results. Median values were used because a normal distribution could not be assumed with a very small sample size.

The output energy was compared against the input energy for each test case and each sensor pairing in a least-squares analysis. The same process as the output energy found the input energy, but in this case, the excitation voltage was constant for the entire frequency interval. The resulting values for input energy are 1.0, 4.0 and 9.0 volts<sup>2</sup> kHz/kHz. The R<sup>2</sup> values for each linear regression are reported in Table 3.

**Table 3: R<sup>2</sup> values for least-squares analysis performed on each test case and each sensor pairing.**

<b>Joint rigidity ratio for each test case</b>	<b>0.08</b>	<b>0.14</b>	<b>0.19</b>	<b>0.20</b>	<b>0.24</b>
<b>Sensor pair: H1V1</b>	0.9989	0.9999	0.9998	1.0	1.0
<b>Sensor pair: H2V2</b>	0.9952	0.9995	1.0	0.9999	1.0
<b>Sensor pair: V1H1</b>	0.9999	0.9999	1.0	1.0	0.9997
<b>Sensor pair: V2H2</b>	0.9994	0.9994	0.9999	0.9998	1.0

All R<sup>2</sup> values are one or very close to one, showing that the output energy to the input energy is linear in all cases.

### 3.6.3. Correlation in $E_j$ with the joint rigidity ratio

Nine  $E_j$  values were computed for each test case (joint rigidity ratio) and each sensor pair. This sample size was small, and again, a normal distribution could not be assumed. The median value was plotted against the joint rigidity value in Figure 17.

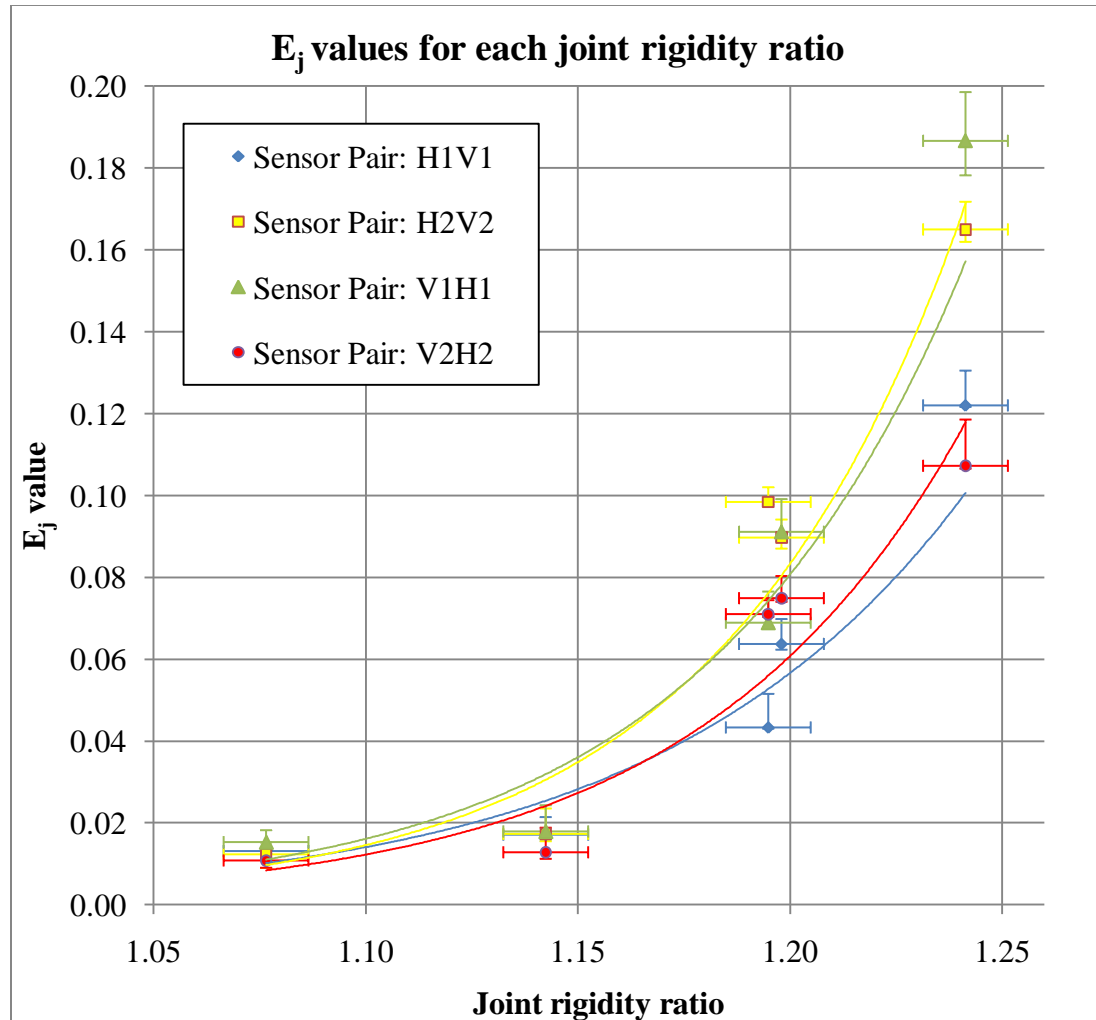


**Figure 17: Plot of  $E_j$  values against joint rigidity ratio values for each sensor pair. Each sensor pairing displays a positive correlation between  $E_j$  and the joint rigidity ratio.**

In Figure 17, the vertical error bars represent a 95% confidence interval based off the median value. These are not symmetric the way a standard confidence interval would be. The horizontal error bars represent a standard 95% confidence interval, which is based off the mean. The relationship between transmitted energy ( $E_j$ ) and the stiffness in the joint (joint rigidity ratio) does not appear to be linear. This could be due to the fact that the joint rigidity ratio is a scaled value from 1.0 to 1.4. At 1.0, the transmitted energy should go to zero. However, the actual joint is supported by brackets and unless the brackets are removed some energy will be transmitted across the brackets. At 1.4, the transmitted energy should reach some maximum. There is no reason to believe that as the joint becomes increasingly stiff, the transmitted energy will increase at a more and more rapid rate. Therefore, it should be expected that at higher values of transmitted energy, the curve in Figure 17 could look more like an 'S' curve.

Some difference in values between sensor pairings is expected due to differences in the bond the sensor makes with the plates, the small differences in size, and the differences in solder material on top of the sensors. The difference in  $E_j$  values by sensor pairing becomes more pronounced as more energy is transmitted. This is likely not due to sources of systematic error like differences in sensor bonding. Since sensitivity in the sensors is frequency dependent, changes in sensor sensitivity could be due to a frequency dependent dampening in the joint that increases as the joint becomes more 'loose'. Unfortunately, from this data it is not really possible to know if this effect is due to sensor characteristics, changes in joint stiffness, or both.

To show the correlation between  $E_j$  and the joint rigidity ratio, some correlation statistics were computed. In Figure 17, an exponential fit was done for each sensor

pairing. Spearman's rank correlation ranks each variable and computes how well the rankings match. The only sensor pair that did not get a 1.0 for Spearman's rank correlation was H2V2. The discrepancy is at joint rigidity values 1.20 and 1.19. This sensor pairing had a slightly higher  $E_j$  value for 1.19 than it did for 1.20. It was mentioned before that these cases have overlapping confidence intervals, making the difference in joint rigidity unreliable. The  $R^2$  values for the exponential fit, and two correlation metrics from the text: Statistical Analysis of Non-normal Data by Deshpande (49) are reported in Table 4.

**Table 4: Correlation statistics by sensor pair between  $E_j$  values and joint rigidity ratios. In all cases, a value close to 1 shows good correlation between variables.**

	Spearman's rank correlation	Pearson's product-moment correlation	$R^2$ value for the exponential fit
H1V1	1.0	0.881494	0.9067
H2V2	0.9	0.931849	0.9137
V1H1	1.0	0.884706	0.8926
V2H2	1.0	0.944084	0.8743

Pearson's product-moment correlation coefficient ranges from -1 to 1 and shows how well the data can represent a line. It is not a traditional linear regression, however. The values for this case are high, but there is little reason to think the data might be linear. On the other hand, there is little reason to think that the data might be exponential either. The  $R^2$  values for the exponential fit are as good as the Pearson's coefficient values. In either case, the correlation between transmitted energy and the joint rigidity is clear.



#### 3.6.4. Summary of results

Wave energy was successfully transmitted across a joint with a rough, dry connection by piezoelectric sensors. The excitation voltage was low, but the transmitted signals were well above the measured noise level for even the loosest joint tested.

Transmitted energy across the joint correlated with measured joint rigidity very well. The relationship appears to be non-linear. The lowest value of Spearman's rank correlation coefficient for any of the sensor pairs was 0.9. This shows very good correlation between transmitted energy and joint rigidity.

The joint design did not allow for really tight test case. This experiment showed more of a 'worst-case' scenario with a joint by having very loose test cases. Those cases showed that the wave energy could be transmitted and correlated with joint rigidity. However, behavior at the other end of the scale has yet to be established.

## CHAPTER 4: EXPERIMENTS CONDUCTED ON SATELLITE

### PNP 1

This chapter describes the second experiment conducted for this thesis. This experiment uses the evaluation method developed in the proof of concept on a functional satellite. In this case, bolt tension is correlated with an energy metric based on the transmitted wave energy of a pulsed signal. The new metric,  $E_r$ , is similar to the energy metric  $E_j$  discussed in Chapter 3.  $E_r$  was developed for this experiment to accommodate specific testing circumstances at the Air Force Research Laboratory Space Vehicles Directorate on Kirtland Air Force Base.

#### 4.1. Goals of the experiment

The experiment was conducted in two phases to assess the utility of the parameter  $E_r$  as a joint quality metric. Torque applied to the connecting bolts in a joint was varied while observing changes in the parameter  $E_r$  in a stationary setting and in-between traditional vibration analysis tests. The goal of the stationary phase was to assess the ability of the energy parameter  $E_r$  to detect changes in joint integrity within acceptable error limits. A secondary goal of the stationary experiments was to test the sensitivity of  $E_r$  to experimental parameters. Repeatability of measurements was also considered. The goal of the second phase, conducted between vibration analysis tests, was to observe changes in the parameter  $E_r$  with changes in joint quality that were known to be invisible to traditional vibration methods. Traditional vibration analysis examines the structure as a whole (2), and can only detect changes in the structure that affect the global stiffness of

the craft. A secondary goal of the second phase was to assess the sensitivity of the energy parameter  $E_r$  to perturbation by vibration. All tests were conducted on a functional satellite to gauge the feasibility of using this quality assessment method under realistic circumstances.

#### 4.2. Equipment and Test Subject

The piezoelectric sensors used to generate and receive the elastic waves in the panels for the experiments conducted with the Air Force Research Laboratory Space Vehicles Directorate were American Piezo Ceramics (Mackeyville, PA) designation APC 850, 7 mm circular wafers, 0.0254 mm thick. Sensors were manufactured with the bottom electrode folded over to the top face so that the sensor could be properly bonded to the structure. Sensors were placed approximately 1cm from the bracket edge as pictured in Figure 18.

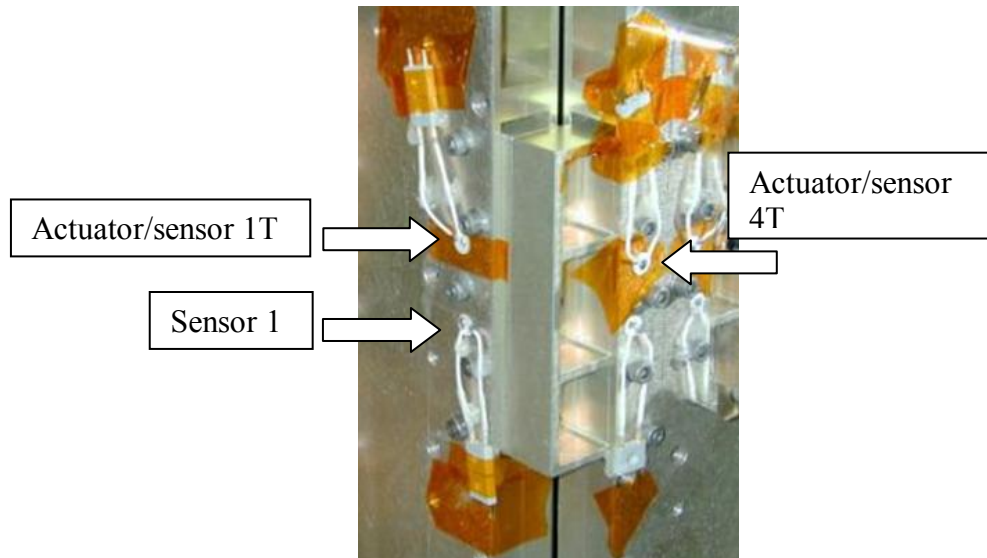


**Figure 18: Location of sensors and actuators on the spacecraft. Sensor 1 was not used as an actuator; it was bonded to the panel with 2319 epoxy.**

Originally, all sensors were bonded with 3M 2319 epoxy. However, the high voltage used to excite the actuating sensors posed a possible threat to sensitive electronics mounted on the satellite panel. The actuating sensors were replaced with identical sensors bonded with cyanoacrylate glue on top of kapton tape. The tape was applied to the panel before the sensors were glued down. A number and the letter 'T' label sensors bonded to the panel in this fashion. This installation method protected the structure from electrical arcing. Three sensor paths were used to collect data: actuator 4T to sensor 1T (4T-1T), actuator 1T to sensor 4T (1T-4T), and actuator 4T to sensor 1(4T-1).

A RITEC RAM 5000™ device was used to generate and receive signals at the piezoelectric actuators/sensors. A National Instruments high-speed digitizer (NI 5102) was used to examine the output signal in the time domain. Frequency sweep settings for the RITEC device were determined from the output signal in the time domain.

#### **4.3. Transmitted energy parameter $E_r$**

The experimental method used for the proof of concept experiment, described in the previous chapter, needed to be adapted for a more complex situation and different equipment. Previously, the method read out the maximum amplitude from a transmitted wave sent continuously for a time interval of 0.01 seconds, and the sensors were excited at 1.0-3.0 volts. The experiments conducted at Air Force Research Laboratory facilities on the satellite designated PnP1 (for Plug-in-Play 1) were to be conducted in conjunction with other experiments. For logistic reasons all experiments used the same sensors and equipment. In addition, it was suggested that the low voltage used in the proof-of-concept method might not have been able to produce a transmittable

signal across the more complex joint geometry. The proof-of-concept method was never tested on the any of the satellite panels at AFRL, and it is unknown if different sensors and a lower voltage could produce satisfactory results.

#### 4.3.1. New experimental parameters

The new smaller, thinner piezoceramic wafer sensors excited at voltages an order of magnitude larger than the voltage used in the proof-of-concept experiment. These sensors were designed to send and receive discrete wave pulses rather than wave trains. The response of the piezoelectric sensor acting as a receiver from a pulse has complicated features in the time domain. Figure 19 shows the received signal at sensor 1 from actuator 4T in the time domain.

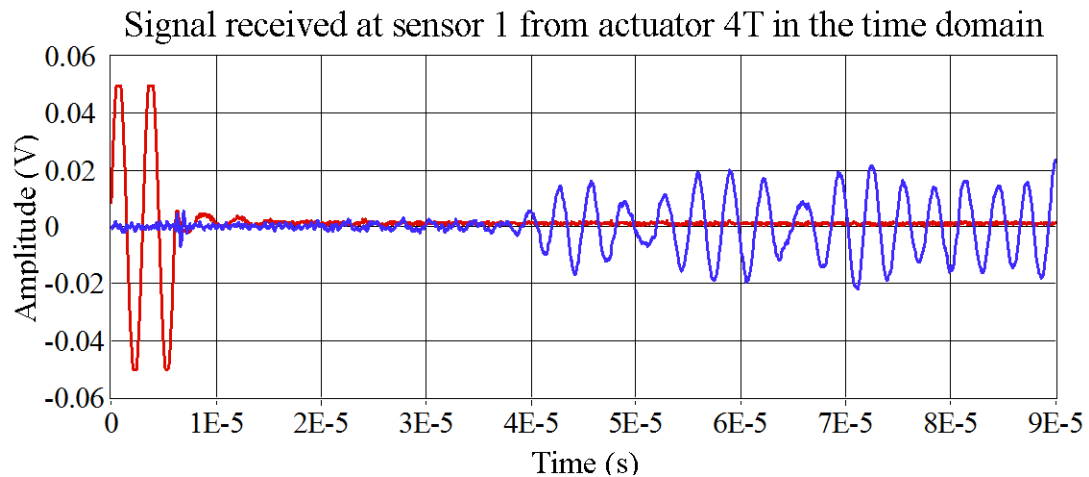


**Figure 19: The red line represents the input signal at actuator 4T. The blue line is the response at sensor 1. This is an example of the shape and character of the received signals.**

The signal in Figure 19 was taken with all bolts in the joint tightened to specification. The input frequency used was 325 kHz, which is near the resonance frequency of the piezoelectric sensor. Therefore, the signal should have a high amplitude

and clear features. From the figure, the ‘first arrival’ pulse lasting from 40 to 50 microseconds is easy to see. However, the remaining features in the signal are less defined. Figure 19 shows an example of the signal under the best circumstances, and it is still not easy to see distinct modes beyond the first arrival.

The dominate type of wave produced in thin plates at the frequencies used in these experiments are Lamb waves (15), which are dispersive. Dispersion characteristics and reflections from obstructions in the panel are possible features in the received signal (3). Although it is difficult to know for certain what features are due to reflections and what are due to Lamb wave (or other type of wave) behavior, because piezoceramic sensors excite waves in plates in a radial direction from the sensor and without preference to mode (15). The amplitude of reflections is more likely due to internal interference of the waves, and not a result of loss of connectivity in the joint. Frequencies present in the signal other than the excitation frequency may be due to noise or dispersion. To be true to the original method, the received signal needed to be filtered to the excitation frequency and the magnitude of the first arriving wave be recorded.

LabView could have controlled the reception and processing of the signals. However, LabView was not installed on the computer controlling the RITEC RAM 5000 at the time experiments were run. Therefore, the software that came with the RITEC device was used to collect the data. All of the required features needed for the test method were already programmed into the frequency sweep function in the RITEC software. As it performs a frequency sweep, it filters out the portion of the signal not at the excitation frequency. Then, it uses an analogue integrator circuit to report the magnitude of a received pulse. Appendix 2 summarizes this process. For most

experiments, the reported magnitude was an average of five consecutive readings at the same frequency. Only a portion of the signal was collected and processed. That portion was determined by the choice of integrator gate delay and width. It is unclear when reflections start appearing in the signal, as evidenced in Figure 19. As a result, some experiments were repeated with different gate widths. The gate delay and several gate widths were determined from viewing the signal in the time domain.

Informal testing was done before experiments were conducted on PnP1 to make sure signals were correctly received and a change in the output of the sweep could be observed with a change in bolt tension.

#### 4.3.2. Equation

The voltage output from a piezoelectric sensor is proportional to the amplitude of the ultrasonic stress wave traveling in the panel (3). Therefore, the energy of the wave for a given frequency is proportional to the square of the amplitude. The data collected for the test method consists of RMS voltages collected for a range of frequencies. The value  $E$  is the area under the curve derived from RMS voltage data. Each RMS value was squared and normalized to a bandwidth. The method used to integrate the discrete data points was the trapezoidal method, and the bandwidth was assumed to be 1MHz.  $E$  was used as a performance metric to compare the energy received at different actuator and sensor pairs in the Results and Discussion section.

$$E = \int_{f_1}^{f_2} \frac{A^2}{\text{bandwidth}} df \quad 21$$

Taking a ratio of  $E$  values for the same range of frequencies for a baseline and a test case give the parameter  $E_r$ . Note that the bandwidth drops out.

$$E_r = \frac{E_{\text{variable case}}}{E_{\text{baseline case}}} = \frac{\int_{f_1}^{f_2} A^2 df_{\text{variable case}}}{\int_{f_1}^{f_2} A^2 df_{\text{baseline case}}} \quad 22$$

$E_r$  is the energy ratio used to quantify the energy transmitted across a joint as the stiffness is changed by loosening bolts. The baseline stiffness is defined as having all bolts at a torque meeting design specification.  $E_r$  values less than one would show a drop in transmission energy across the joint.  $E_r$  is similar to the energy parameter  $E_j$ , but different in that  $E_j$  was not a ratio in reference to a baseline but a portion of the excitation frequency.

The formulation of  $E_r$  is dependent on consistency in the data. Care was taken to ensure that all equipment settings (integrator rates, frequency steps, and so on) were the same for the variable case and the baseline case and that all equipment was given time to warm up to help reduce hardware error.

LabView programs were written to extract the text data obtained with the Ritec RAM 5000 and analyze it with the above methods. Appendix 3 contains documentation on those programs.

#### 4.4. Procedure

Data was taken for panel-to-panel connections tightened to specification at 2.7 Nm and for values below specification (1.8, 0.9, and 0 Nm). The experiment was conducted in two phases. The first phase was conducted with the satellite in a stationary setting, and the second phase was done in conjunction with vibration tests. The bolts that were loosened and retightened are described below in Figure 20. The first phase of the



experiment loosened and tightened all three bolts evenly. The second phase of the experiment only adjusted the bottom bolt.

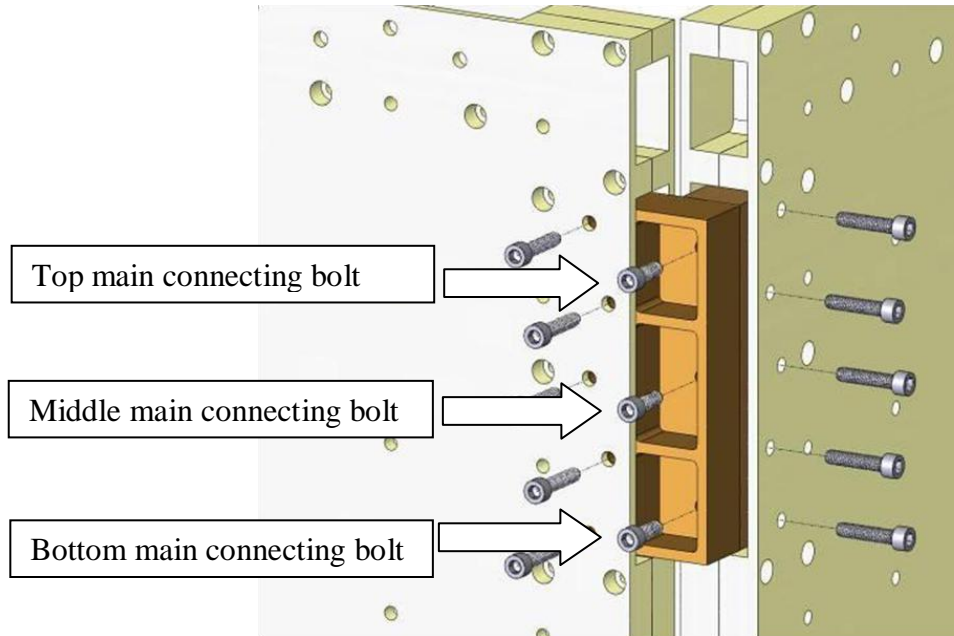


**Figure 20: The bracket assembly contained 13 bolts. Only the three main connecting bolts shown were adjusted during the experiment.**

A RITEC RAM 5000™ device was used to generate and receive signals at the piezoelectric actuators/sensors. An actuator was placed on one side of the panel-to-panel connection and the sensor on the other side (Figure 19). The input pulse was a 3-cycle sine wave burst at 125 Volts (peak-to-peak) repeated at a rate of ten bursts per second. The RITEC device swept through a frequency range from 250 kHz to 450 kHz in 1.0 kHz steps. Frequencies lower than 250 kHz tended to damage the sensors. The dispersion curves for aluminum predict higher order modes occurring at a frequency and thickness product above one (15). The frequency distance product for the panel ‘skin’ at 450 kHz was 1.06. Higher order modes would further complicate the signal, so we chose our

upper frequency limit to be 450 kHz. At each frequency, the RMS voltage was measured. The reported amplitude (RMS voltage) at each frequency step was an average of five consecutive readings. The gate settings discussed next determined the integration time.

The gate delay and widths for the integrator circuit were determined after analyzing the output from a National Instruments high-speed digitizer (NI 5102). The integrator gate delay was set at 30  $\mu$ s. This was after the excitation but before any significant signal arrived at the sensor. The gate widths were selected so that the sensor captured the first incoming signals but rejected signals that arrived much later. Later signals were unwanted because they may incorporate reflections and other noise from features of less interest. The ideal gate width was not known exactly, so three different widths were investigated: 20 $\mu$ s, 50 $\mu$ s, and 80 $\mu$ s. The width with the greatest sensitivity to bolt torque changes was assumed to incorporate signals from the most relevant region of interest.

#### **4.4.1. First phase of the experiment: craft held stationary**

All measurements were taken while the satellite was secured to a workbench. The bolts connecting the bracket were originally tightened to 2.7 Nm. A full set of data constituted nine frequency sweeps collected on all three sensor paths, each with all three gate settings. Data was collected after each of the following torque settings were applied evenly to the three main connecting bolts: 2.7 Nm (baseline), 0 Nm (loose), 0.9 Nm, 1.8 Nm, and 2.7 Nm. 'Loose' or zero Nm is defined as loosening the bolts to the point where gapping initiates between the bolt head and the structure.

#### **4.4.2. Second phase of the experiment: craft perturbed by vibration**

This experiment was done in conjunction with vibration tests. The experiment took place while the satellite was seated on the vibration table in-between periods of perturbation by shaking. The goal of this experiment was to see if one loose bolt could be detected by the method and if the results of the test would be affected by vibration.

All three integrator gate settings were taken for one sensor pair: sensor 4T-1. After the baseline data was obtained, the satellite was shaken at 2.0  $g_{rms}$  (spectrum unknown) as part of a vibration test. A second baseline was taken for repeatability. The bottom bolt (of the three described in the first experiment) was loosened to zero Nm, and data was taken for the damaged case. After the satellite was vibrated again with a loose bolt, more data was taken for the post-vibration damaged case to see any further changes to the  $E_r$  value. The final data set was collected when the bolt was re-tightened. The post-vibration baseline was used as a reference, although either baseline would have given similar results.

#### **4.5. Results and discussion**

This section presents the results of both phases of the experiment, followed by a brief summary of the results.

##### **4.5.1. Phase one: craft held stationary**

Table 5 shows the  $E_r$  values at a 2.7 Nm torque setting for all three sensor paths and all three gate duration settings. All of these values should be nearly 1.0 to show that the transmission energy has returned to levels comparable to baseline levels. The largest

deviation is 12.3%. This indicates that a drop in  $E_r$  less than 12.3% is not necessarily a valid indication of a loose joint. This 12.3% deviation also provides a crude measure of the test repeatability. However, this value is determined based on the results of sensor pair 4T-1.

**Table 5:  $E_r$  values after loosening and returning the bolts to design specification. The sensor pairs are given as “actuator, sensor”. The largest deviation from baseline is 0.877, at sensor pair 4T-1 at the 20  $\mu$ s gate duration. This shows a repeatability of 12.3% at 20  $\mu$ s, although the repeatability at 50  $\mu$ s appears to improve to 5.7%.**

Width of time window ( $\mu$ s)	Sensor path: 4T-1T	Sensor path: 1T-4T	Sensor path: 4T-1
20	0.9442	0.9778	0.8767
50	0.9948	0.9476	0.9430
80	0.9226	0.8995	1.069

Sensor pair 4T-1 appears to be sensitive to the gate width when the bolt is tightened to specification (Table 5) but less sensitive at other torque settings as shown in Table 6. Additionally, this data was used to establish the best gate width. At the 50  $\mu$ s gate width, the crude repeatability would be 5.7%, based on the maximum deviation from  $E_r = 1.0$ .

**Table 6: Variation in  $E_r$  by gate widths for the 1.8 Nm preload test-case at sensor pair 4T-1.**

gate width ( $\mu$ s)	$E_r$
20	0.7474
50	0.8228
80	0.8282

The repeatability may also be influenced by the torque measurement. The error listed on the torque wrench used in the experiment was +/- 6%. The actual error associated between torque values may vary from what is listed on the tool due to

influence of error from operator, tool alignment, thread resistance, etc. One source listed the compound error associated with a torque wrench at +/- 25%(50).

Table 7 shows  $E_r$  values for the 50  $\mu$ s gate width. The drop in  $E_r$  could be used to discern a 0.9 Nm applied torque from baseline for all three sensor paths. However, sensor path 4T-1 is the only path with an  $E_r$  value able to show a drop in transmission greater than 12.3% for a preload of 1.8 Nm. The  $E_r$  values for gate width settings 20 and 80  $\mu$ s (not shown) on sensor pairs 4T-1T and 1T-4T could not discern the 0.9 Nm torque setting from the baseline. In contrast, sensor pair 4T-1 was successful in showing a drop in  $E_r$  for a 1.8 Nm preload for all gate widths as presented in Table 6.

**Table 7:  $E_r$  values for all three sensor paths for a 50  $\mu$ s gate setting. All three sensor paths show a drop in transmission energy from baseline for the loose and 0.9 Nm test cases. Only sensor path 4T-1 shows a significant drop in energy from baseline for a 1.8 Nm preload indicating that the sensor path is more sensitive to changes joint stiffness.**

Test-case	4T-1T	1T-4T	4T-1
<b>baseline</b>	1.000	1.000	1.000
<b>0 Nm</b>	0.003512	0.004608	0.0007427
<b>0.9 Nm</b>	0.7633	0.7481	0.5794
<b>1.8 Nm</b>	0.9519	0.9287	0.8228
<b>2.7 Nm</b>	0.9948	0.9476	0.9430

$E_r$  is always relative to the baseline taken for a specific sensor path, and not useful when comparing the performance of different sensor paths. Instead, E (Equation 21) is used to compare the performance of each sensor pair. These values, listed in Table 8, show a marked increase in energy for sensor pair 4T-1. The larger energy values translated to greater test sensitivity as shown in Table 7. The exact reason for the difference in performance is unknown. It is possible that some unseen obstruction is

responsible for the difference in signal strength, but a more likely reason is the Kapton tape used under receiving sensors 4T and 1T, which is expected to absorb some energy of the elastic wave.

**Table 8: Variation in baseline E values detected at sensors by time window width and sensor path. The pattern repeats in other test cases. The longer gate width captures more of the return signal, but in all cases sensor 1 detects greater transmitted energy. The likely reason 4T is the bonding method used to fix the sensor to the panel. The units are (RMS Voltage)<sup>2</sup>.**

Time window width ( $\mu\text{s}$ )	4T-1T	1T-4T	4T-1
20	3.982	4.046	13.26
50	106.4	108.2	170.4
80	180.3	183.2	462.6

#### 4.5.2. Phase two: craft perturbed by vibration

The following table presents data collected in the second phase of the experiment. These results show that a loose bolt was easily detected with an  $E_r$  that was 40% of baseline. The test technique measured the  $E_r$  equally well before and after vibration and showed a return to normal readings when the bolt was re-tightened to specification. The pre-vibe baseline was within 4.3% of the post-vibe baseline.

**Table 9: Sensor pair 4T-1 with a 50  $\mu\text{s}$  gate duration. The post-vibration baseline was used in the calculation of  $E_r$ .**

Test condition	$E_r$
baseline pre-vibration	1.043
baseline post-vibration	1.000
loose bottom bolt pre-vibration	0.3953
loose bottom bolt post-vibration	0.3951
bottom bolt re-tightened	0.9748

From the values in Table 9, vibrating the joint between measurements has little effect on the value of  $E_r$ . We expected some change when the craft was shaken due to slight shifting from components and panel interfaces along with the possibility of the tape disbond underneath the sensors. However, no such change was detected. The redundancy in the design may keep the bracket from shifting during vibration even with one loose bolt. Loosening the bottom bolt had no detectible effect on the global stiffness of the craft according to technicians, yet the test method clearly shows a drop in transmission energy of about 60%. Although this level of damage may have insignificant influence on the control or stiffness of the structure, it shows the utility of this method for detecting minute changes in a spacecraft structure compared to a known good baseline. This system has the potential to rapidly assess the joint integrity of a spacecraft or spacecraft components before launch.

#### **4.5.3. Summary of results**

This research was one of the first structural health monitoring experiments on a functional satellite. The test technique was able to detect loose bolts in a panel-to-panel connection with high fidelity. Global stiffness measurements typically conducted on satellites as part of prelaunch testing were not able to detect the loose bolts.

The first experiment showed a high correlation between relative energy transmission across the panel-to-panel connection and bolt torque. The most sensitive sensor pair was able to distinguish an applied bolt torque 0.9 Nm less than specification. The other, less sensitive, sensor pairs transmitted lower amplitude values. The bonding method used for the receiving sensors appears to decrease the measured energy. Higher

excitation amplitudes or bonding the receiving sensors directly to the structure with epoxy may correct this. The first experiment also showed that the gate width setting is important in improving the sensitivity and the repeatability of the measurement.

The second experiment showed that the test could easily indicate if only one bolt was loose. Results also showed that vibrating the spacecraft between measurements does not significantly affect the readings between identical configurations.

Both experiments showed that the test technique was able to detect the relative torque on a bolt with repeatability of 5.7% when using an appropriate integrator gate width for the region of interest.



## CHAPTER 5: EXPERIMENTS CONDUCTED ON SATELLITE PNP2

The previous experiment established that detecting loose bolts by measuring  $E_r$ , a parameter based on wave energy, was possible. This experiment attempts to determine the limitations of the test by investigating the repeatability and the range a single sensor pair.

### 5.1. Goals of the experiment

The experiment was conducted on two satellite panels, joined together by three brackets. The panels did not have any hardware or other functional components attached to them. These panels were a slightly different design than the panels used in the experiments described in Chapter 4 (PnP 1). The bracket connecting the panels was larger, but less complicated. The following experiment was intended to evaluate the utility of the ultrasonic test method developed in the previous chapter by finding the repeatability of the test and the range where the test is valid.

### 5.2. PnP 2 panels and location of sensors

The image in Figure 21 shows the panels designated PnP 2. These were very similar to the panels used on satellite PnP 1, but they are larger and do not have any equipment or components attached to them.

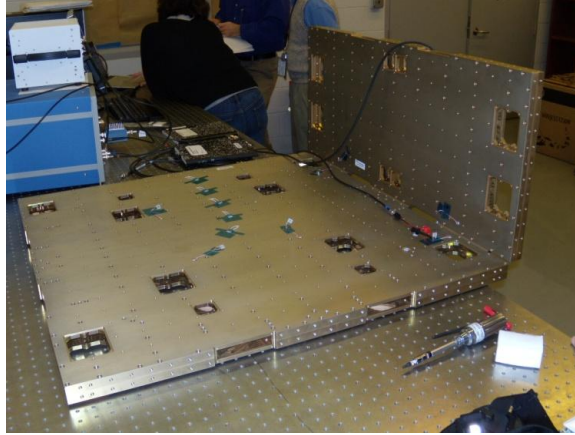


**Figure 21: Panels designated PnP2.**

The smaller panel is joined to the larger panel by three brackets as shown schematically in Figure 22.

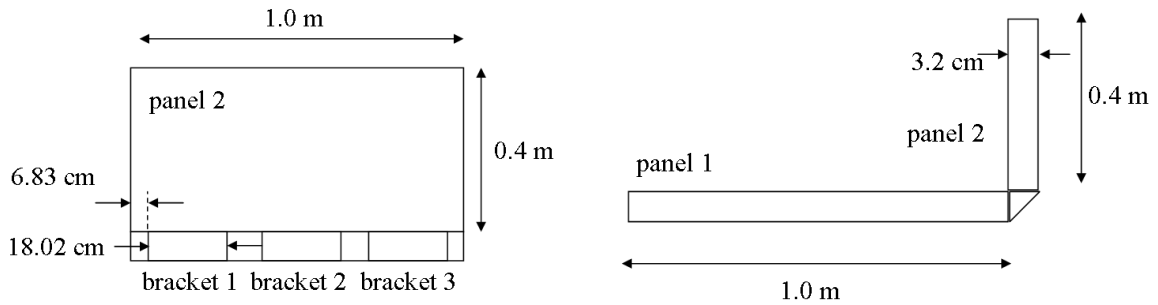


**Figure 22: Diagram of the PnP 2 satellite panels showing the bracket layout on the panels.**

Like the panels on satellite PnP 1, the PnP 2 panels do not touch. Wave transmission occurs through the brackets. Only Bracket 1 from Figure 22 is used in this experiment. Informal investigations conducted on these panels before official tests began confirmed that adjusting bolts on brackets 2 and 3 did not change the output waveform received at sensor 7 from sensor 4 to any degree. Energy values (the metric  $E_r$  from PnP

1 experiments) also did not show any change from the baseline case when bolts on brackets 2 or 3 were adjusted.

The PnP 2 bracket design is far more simple than the design used for PnP 1, however, it is larger. Figure 23 pictures bracket 1. Bracket 1 contains 18 bolts. Nine bolts connected the bracket to the Panel 2 and nine bolts connected the bracket to Panel 1.



**Figure 23: Bracket one as seen from the back side of the panel.**

These bolts were numbered in order from top to bottom, left to right as shown in Figure 24.

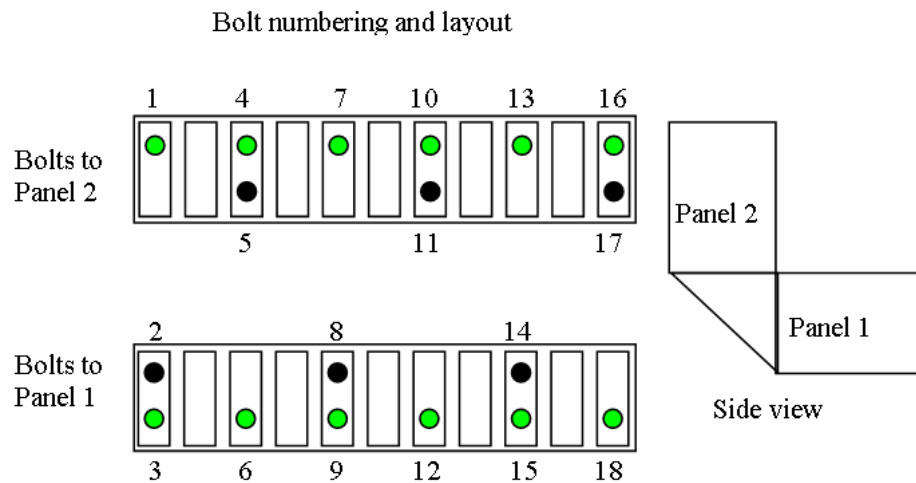


**Figure 24: Bolt numbering scheme for Bracket one.**

The bolts located in the corner of the bracket could not be adjusted without removing another bolt. For the sake of continuity in some of the tests, only the bolts on the outside edges of the bracket were adjusted. These bolts are colored green in Figure 24. These panels were used for other experiments by other researchers; so many sensors were actually attached to the panel. The sensors pictured above were the only sensors used for this experiment. They are labeled S4 and S7, as pictured in Figure 25. The sensor shown on Panel 1, attached to leads is S4.

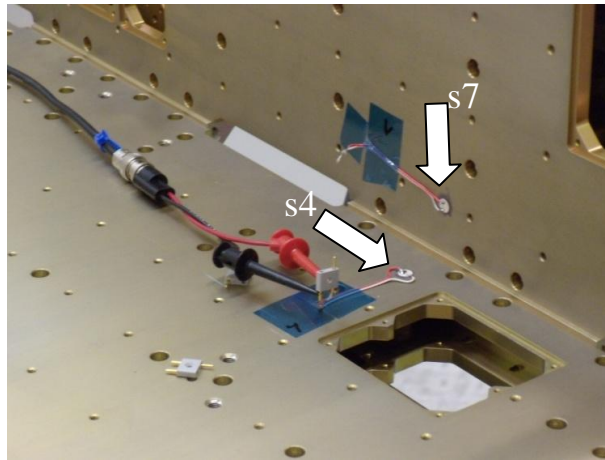


**Figure 25: Location of the sensors. In all tests, S4 was used as the transducer and S7 was used as the receiving sensor.**

The following table lists the horizontal distance from the sensor path to each bolt. this was useful for determining the range of the sensors. Additional information on Bracket 1 and the layout of the sensors is in Appendix 6.

**Table 10: Horizontal distance from each bolt to the sensors. The sensors were located just to the right of bolt numbers 10 and 12.**

<b>Bolt numbers</b>	<b>Horizontal distance from sensors</b>
<b>10,12</b>	0.03
<b>13,15</b>	3.24
<b>7,9</b>	3.31
<b>16,18</b>	6.51
<b>4,6</b>	6.68
<b>1,3</b>	9.85

### **5.3. Procedure**

The following tests targeted the repeatability and the range of the test in two phases. Different torque wrenches were used for each phase. The first phase used a torque wrench that released when the desired torque was reached. The dial on this torque wrench is difficult to read and it has a high degree of error associated with it making the torque measurement inaccurate. However, it was only adjusted once, so repeated applications of torque to the bolts were very precise. Accuracy was more important in the second phase, so a digital torque wrench with a smaller error was used. However, it did not release when the desired torque was reached, so some precision was lost.

#### **5.3.1. Repeatability tests**

The torque wrench (by Craftsman) that was used for the first set of experiments reports an error associated with the tool to be +/- 6%. All other equipment is as described in Chapter 3. The markings on the torque wrench are difficult to read, so multiple

adjustments could result in higher error. This torque wrench was adjusted to 3.2 Nm only once, at the beginning of the experiment, in an effort to reduce error.

All 18 bolts were preloaded to 3.2 N-m. Tests were then taken to determine appropriate equipment settings. The settings used for this phase of the experiment were a gate delay of 60 $\mu$ s, a 30 $\mu$ s gate width, and a frequency range of 250 to 350 kHz. The frequency range was chosen after looking at output corresponding to 150 kHz to 500 kHz. The largest response was near 300 kHz. After examining time domain signals taken at 250 and 350 kHz, the gate delay and width were chosen.

After an initial measurement was taken at the above settings, Bolt 1 was loosened. As in previous chapters, a loose bolt is defined as a bolt loosened past the friction point so that it is able to rotate freely in the bolt-hole. A measurement was taken while the bolt was loose. The bolt was retightened to 3.2 N-m. This process was repeated three times before moving onto the next bolt. The bolts that were tested in this manner are numbers 1,3,4,6,7,9,10,12,13,15,16, and 18. From Figure 23 and Figure 24, bolts 2, 5, 8, 11, 14, and 15 were located on the innermost portion of the joint. These bolts could not be adjusted without removing other bolts. For the sake of continuity, testing of these bolts was omitted.

### **5.3.2. Range tests**

For the range tests, the longer frequency range and a shorter time window were used. The frequency range was 250-500 kHz, the time window started after a delay 50  $\mu$ s and lasted for 30  $\mu$ s.

For this test, a DTW 265i digital torque wrench was used to adjust the bolts. The reported error associated with the tool was clockwise +/- 2.5%, counterclockwise +/- 3.5%. The resolution was 0.01 N-m. The minimum setting, however, was only 1.6 N-m. Bolt preload values between this setting and loose were not tested.

Before beginning tests on individual bolts, all 18 bolts were adjusted to 3.2 Nm. Data was collected, then all 18 bolts were adjusted to 2.9, 2.7, 2.3, 1.8, and 1.6 Nm. Data was collected at each step. This was done to test the response of the joint as a whole.

Three trials at each of the following values of preload were tested: 3.2, 2.9, 2.7, 2.3, 1.8, 1.6, and 0 Nm. These values were tested at each bolt, one at a time. Data was collected at each step.

After a brief inspection of the results, the frequency range was changed from 250-500 kHz to 150-500 kHz, and the time window was returned to a 60  $\mu$ s delay with a 30  $\mu$ s duration. The test was repeated with one trial per bolt adjustment.

## **5.4. Results and discussion**

This section reports on the data collected for both phases of the experiment. Some of the data was collected with different equipment settings. All settings are reported with the accompanying description of the data to avoid confusion.

### **5.4.1. Short-term repeatability**

How repeatable this joint assessment metric is will be determined by how well the metric returns to a baseline value after a variable is changed and then returned to its original state. The variable tested, in this case, is bolt preload. The metric to be

examined for repeatability is  $E_r$ . However,  $E_r$  is in reference to a baseline. Arbitrarily, the first data point could be used as a baseline for all subsequent measurements. However, this approach makes the data analysis more confusing. Instead, the data analysis for this phase of the experiment uses energy values (E) first described in Equation 21. These values have units of  $\text{volt}^2$ .

The following table lists values of E obtained at each bolt for three to four trials. In this table, the percent difference is used to show the similarity between energy values collected at each bolt.

**Table 11: Energy values (E) for each bolt number. The units for these values are  $\text{volt}^2$ . This data was collected with the following equipment settings: frequency range of 250-350 kHz and a time window with a 60  $\mu\text{s}$  delay and 30  $\mu\text{s}$  duration.**

Trial	bolt 1	bolt 3	bolt 4	bolt 6	bolt 7	bolt 9
1	0.01277	0.0128	0.01278	0.01277	0.01268	0.01251
2	0.01272	0.01282	0.01278	0.01263	0.01252	0.01199
3	0.01275	0.01281	0.01272	0.01247	0.01255	0.01236
4						
<b>Median value</b>	0.01275	0.01281	0.01278	0.01263	0.01255	0.01236
<b>% Difference</b>	0.42%	0.20%	0.42%	2.36%	1.26%	4.25%

**Table 11: Energy values (E) for each bolt number (continued).**

Trial	bolt 10	bolt 12	bolt 13	bolt 15	bolt 16	bolt 18
1	0.01232	0.01236	0.01125	0.01071	0.01066	0.01081
2	0.01214	0.01181	0.01087	0.01055	0.01072	0.01101
3	0.01218	0.01153	0.01089	0.01052	0.01084	0.01097
4						0.01083
<b>Median value</b>	0.01218	0.01181	0.01089	0.01055	0.01072	0.01097
<b>% Difference</b>	1.45%	7.04%	3.47%	1.88%	1.67%	1.78%



The data set was small, so median values were used instead of averages. The percent difference reported in Table 11 was computed by taking the difference of the minimum value from the maximum value and dividing it by the median. The largest percent difference was 7.04%. It is no surprise that it occurred at a bolt directly under the sensors. Likewise, the smallest percent difference, 0.20%, occurs at a bolt located farthest from the sensor. Proximity to the sensors should influence the sensitivity of the test. This is shown again in the second phase of the experiment.

A demonstration of repeatability for Bolt 13 is shown in Figure 26. The repeatability for Bolt 13, as given by the % difference is 3.5%. This plot demonstrates repeatability visually, by showing the output of the receiving sensor for each ‘tight’ case and each loose case taken between tight cases. The system returned to previous conditions three times within a difference of 3.5%.

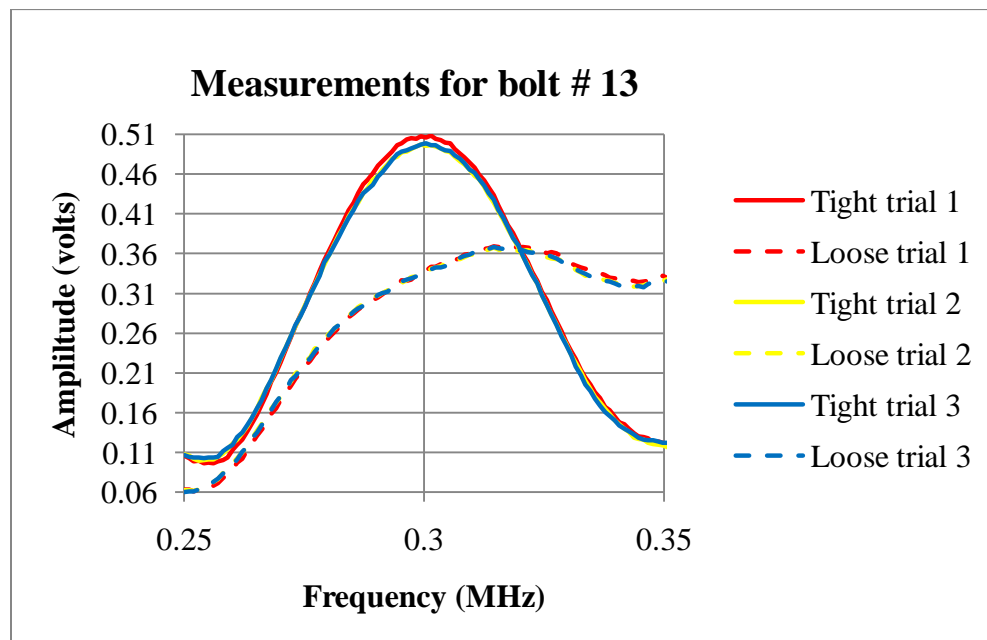


**Figure 26: Repeatability for Bolt 13.** The above plot shows three trials at 3.2 Nm preload and the in between loose cases. This data was collected with the following equipment settings: frequency range of 250-350 kHz and a time window with a 60  $\mu$ s delay and 30  $\mu$ s duration.

### 5.4.2. Long-term repeatability

In all cases presented in Table 11, all of the bolts in the bracket are preloaded to 3.2 Nm. Therefore, they should be able to demonstrate some repeatability. Figure 27 shows the baseline energy values from Table 11 in the order they were taken. The labels on the abscissa are a number followed by a letter. The number indicates the bolt number and the letter is the trial number. Trial 1 is a, 2 is b, 3 is c, and so on.

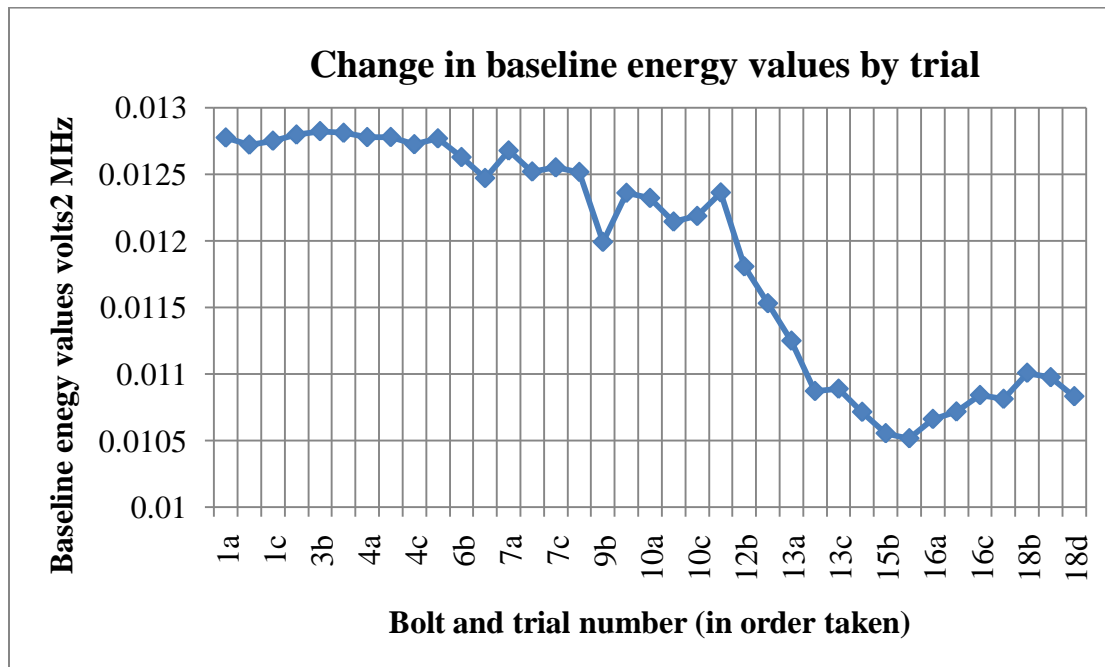


**Figure 27: Values from Table 11 plotted in order taken. The change in energy from the start of the test to the end is a 15% reduction. This data was collected with the following equipment settings: frequency range of 250-350 kHz and a time window with a 60  $\mu$ s delay and 30  $\mu$ s duration.**

There is a distinct drop in E as the test progressed. Overall, there was a 15% loss in energy. It appears that there is a cumulative effect. As bolts are adjusted, they are damaged. As a result of this damage, or error in the way the bolt is adjusted (with the torque wrench or operator of the torque wrench), the bolts may not seat themselves in exactly the same location as before. This can lead to small changes in the joint that could

result in an increase or decrease in transmitted wave energy. Decreases are more likely because damage to the threads on the bolt would cause a loss in preload.

Also, the plot in Figure 27 shows that the largest losses or gains in E values occurred at bolts closest to the sensor (bolts 7, 10, 12, and 13). After examining the values in Table 11, this is expected.

This shows that the test is sensitive to small amounts of damage, but is therefore not repeatable in the long term. However, the number of times the bolts in this bracket were adjusted is well outside what would be considered normal use for a satellite panel. Normal use might consist of adjusting the bolts one to three times in the course of assembly and testing for flight. Therefore, being sensitive to small amounts of damage might be advantageous.

More to the point, this data shows a trend that suggests that it is under the influence of another variable. That variable is likely induced damage from multiple trials, but could also just be a function of the location of the bolts. In any case, the values in Table 11 cannot all be averaged and used as a baseline for all tests conducted on that bracket. This data shows that for the second phase of the experiment, the baseline chosen for each bolt adjustment should be a value obtained recently, and for that bolt number.

### **5.4.3. Range**

$E_r$  values were calculated with the median of the three 'loose' trials divided by the last baseline case tested. For example, when all testing for Bolt 4 was completed, the bolt was returned to a 3.2 Nm load. Data was taken before any adjustments to Bolt 6 were

made. This value was used as a baseline for all measurements taken with Bolt 6 as a variable case.

An  $E_r$  value of 1.0 would indicate that the variable case is no different from baseline. Figure 28 shows the difference of  $E_r$  values and 1 for test cases where a single bolt was loose.

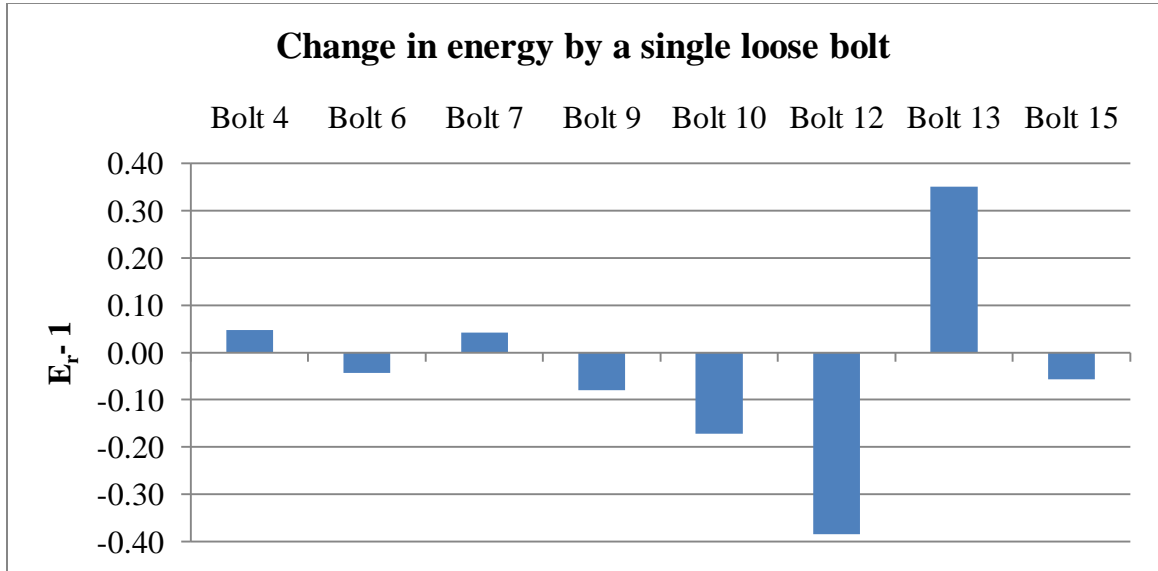


**Figure 28: Change in energy (as shown by the difference in  $E_r$  from 1) by a single loose bolt. This data was collected with the following equipment settings: frequency range of 250-500 kHz and a time window with a 50  $\mu$ s delay and 30  $\mu$ s duration.**

The largest change occurred at bolts close to the sensor. Bolt 13 showed a dramatic increase in energy transmission when the bolt was loosened. This is unexpected and contrary to the idea that loss in pre-load results in a loss in contact area which results in a loss in transmitted energy. The increase is 30% over baseline, is not insignificant enough to discount as an anomaly. The increase could be due to a change in stress distribution near the sensor as a result of loss in preload in a nearby bolt. The internal roughness and contours of the bracket would certainly play a part in that case. This could

also be due to wave scattering and subsequent constructive interference inside the bracket. The increase in energy could be used as a valid indicator of joint integrity, but it is unknown what determines how a loose bolt will present itself in the data set. There may be multiple factors, and therefore if a value above or below baseline is possible, a in-between is possible also. This would make the test unreliable.

However, the results appear to be dependent on equipment settings. Figure 29 shows improved results with different equipment settings. The longer frequency range, the shifted time window, or a combination of both is responsible for the improved results.

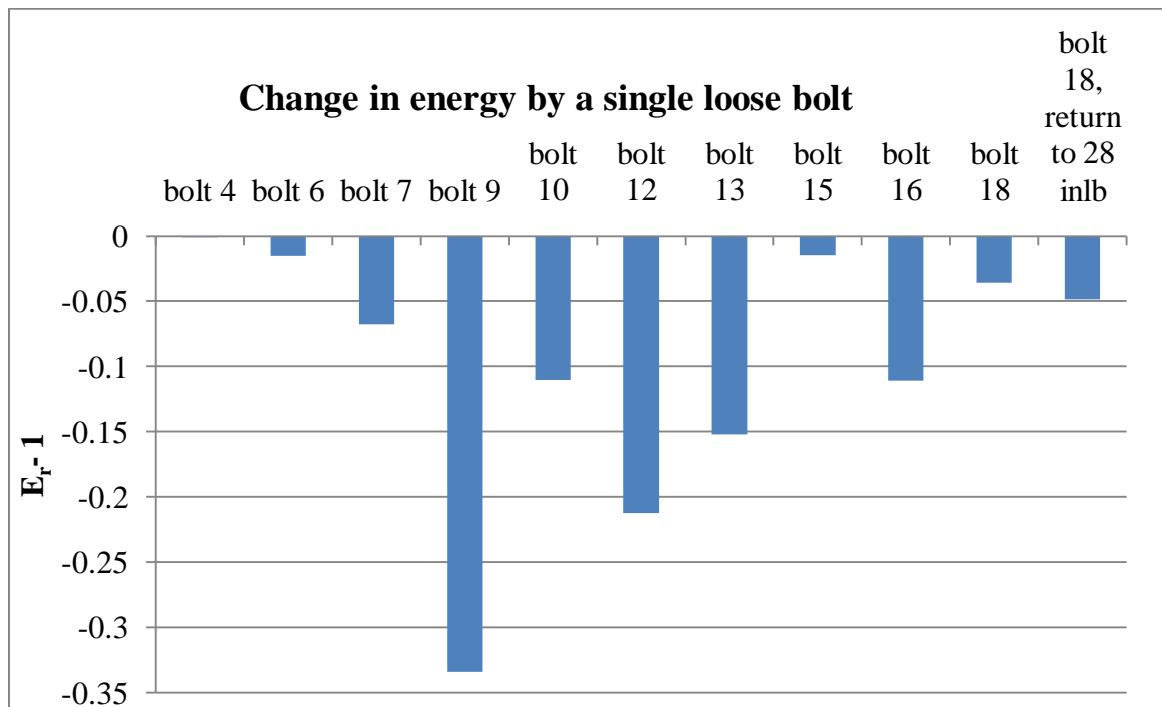


**Figure 29: Energy change with loose bolts with the following equipment settings: frequency range of 150-500 kHz and a time window with a 60  $\mu$ s delay and 30  $\mu$ s duration.**

From Figure 29, the largest response to a loose bolt occurred at Bolt 9, followed by Bolt 12, and then Bolt 13. The smallest response was for Bolt 4, Bolt 3, and Bolt 1.

The latter two are not shown as their response was negligible. The last value in the plot is the final value recorded after Bolt 18 was returned to a 3.2 Nm preload.

Although Bolts 6 to 18 all showed some drop in energy from baseline when loosened, a small change in energy may not be enough to signify a loose bolt. When Bolt 18 was re-tightened, the energy value went down slightly which is not expected. This suggests that any change from baseline less than 5% may not be valid. Previous tests suggested that the repeatability of the test might be as large as 7%, so this makes sense.

To the left, Bolts 7 and 9 showed a response greater than 5%. From Table 10, they are 3.31 cm away, horizontally, from the sensors. To the right, Bolts 13 and 16 showed a response greater than 5 %, but Bolt 15 did not. Bolt 15 is located with Bolt 13 at 3.2 cm away from the sensors. Conservatively, this suggests that the sensor have only a maximum of a +/- 3 cm range in the horizontal direction.

The next set of data is intended to show the range of the test in terms of variable preload. Unfortunately, this data was collected with the same settings as the data presented in Figure 28. This data is less reliable, but does show that a single bolt tightened to a value less than specification (3.2 Nm), but more than loose is detectable.

**Table 12: Energy values for the bracket when all 18 bolts were adjusted to a variable preload. The equipment settings for this data were: frequency range of 250-500 kHz and a time window with a 50  $\mu$ s delay and 30  $\mu$ s duration.**

Average bolt preload (Nm)	Energy (volt <sup>2</sup> )	E <sub>r</sub>	E <sub>r</sub> -1
0.6	7.53E-03	0.6847	-0.3153
1.8	8.75E-03	0.7963	-0.2037
2.3	1.12E-02	1.0159	0.0159
3.2	1.10E-02	1.0	0

The sensors were able to detect a 1.4 Nm loss in preload when all bolts were adjusted equally. Higher values were not detectable by this method at these equipment settings. From these results, values of preload higher than 1.8 Nm were not expected to be detectable as less than 3.2 Nm for a single loose bolt.

Table 13 shows the change in  $E_r$  from 1 ( $E_r-1$ ) for each bolt as it was loosened to a variable torque, shown in the left column. Bolt 12, highlighted in red, gave the most consistent response and showed a change in energy from baseline greater than 5% at 2.7 Nm.

**Table 13: Change in  $E_r$  from 1 ( $E_r-1$ ) for each bolt as it was loosened to a variable torque. The equipment settings for this data were: frequency range of 250-500 kHz and a time window with a 50  $\mu$ s delay and 30  $\mu$ s duration.**

	<b>bolt 4</b>	<b>bolt 6</b>	<b>bolt 7</b>	<b>bolt 9</b>	<b>bolt 10</b>	<b>bolt 12</b>	<b>bolt 13</b>	<b>bolt 15</b>
<b>loose</b>	0.05	-0.04	0.04	-0.08	-0.17	-0.38	0.35	-0.06
<b>1.6</b>	0.01	-0.02	0.03	0.09	0.11	-0.20	0.02	-0.14
<b>1.8</b>	0.01	-0.01	0.03	0.00	0.06	-0.16	0.00	-0.10
<b>2.3</b>	0.01	0.00	0.00	0.02	-0.02	-0.09	0.01	-0.08
<b>2.7</b>	0.00	0.00	-0.01	-0.03	-0.03	-0.02	0.01	-0.07
<b>2.9</b>	0.01	-0.01	-0.02	-0.05	0.00	0.02	0.01	-0.06

When the bolts were adjusted one at a time, the largest loss in preload was 0.05 Nm (at 2.7 Nm). This was better than expected, even with less than desirable equipment settings.

#### 5.4.4. Summary of results

How repeatable this joint assessment metric is will be determined by how well the metric returns to a baseline value after a variable is changed and then returned to its original state. For each bolt, the largest percent difference was 7.04% for three trials.

This shows good repeatability for a small number of trials. There is a distinct drop in E

as the test progressed. Overall, there was a 15% loss in energy. It appears that there is a cumulative effect. As bolts are adjusted, they are damaged. This shows that the test is sensitive to small amounts of damage, but is therefore not repeatable in the long term. As large numbers of adjustments are outside of normal use for a satellite, being sensitive to small amounts of damage might be advantageous.

This data shows a trend that suggests that it is under the influence of another variable. These values could not be averaged. The remaining tests were computed with the baseline obtained most recently

The repeatability tests showed evidence of the sensitivity of the sensors being dependent on proximity to the bolt being tested. The largest percent difference reported in Table 11 was for a bolt closest to the sensors. Likewise, the smallest percent difference was for a bolt located farthest from the sensor.

With a frequency range of 150-500 kHz, all loose bolts except numbers 1,3, and 4 were detected. Based on a drop in transmission greater than 5%, a conservative estimate for the maximum range for the sensors is +/- 3.0 cm. This range is valid for this joint geometry and specific placement of sensors.

An adjustment to Bolt 12 of 0.5 Nm less than baseline (3.2 Nm), which is directly under the sensors, was detectable by this assessment method. This was better than expected, based on a test where all 18 bolts were adjusted evenly. The equipment settings were less than optimal, suggesting that these results could be improved.



## CHAPTER 6: CONCLUDING REMARKS

### 6.1. Proof of concept experiment allowed the project to move forward.

The proof of concept experiment was successful in the respect that it was able to show a correlation between joint rigidity and energy transmission for sample joint cases with a range of measured rigidity values. However, it was limited to the energy transmission due to harmonic excitation. A methodology to experimentally determine the rigidity of a joint was developed and associated errors were discussed. From this test design, the scope and complexity of the larger problem became apparent. Despite a very complicated signal, transmitted energy across the joint correlated with measured joint rigidity very well. The lowest value of Spearman's rank correlation coefficient for any of the sensor pairs was 0.9. This shows very good correlation between transmitted energy and joint rigidity. The relationship appears to be non-linear. The lessons learned from this test were used in the next set of tests on real satellites.

### 6.2. These Responsive Space Initiative Project goals were met by experiments done on PnP1 and PnP2.

The experiment done on satellite PnP1 was one of the first structural health monitoring experiments performed on a functional satellite. This shows the utility of the test under realistic conditions. The test technique was able to detect loose bolts in a panel-to-panel connection with high fidelity, so the primary goal of designing a structural quality assessment was met.

For all of the loading conditions, the drop in energy transmitted across the joint correlated with a drop in measured joint rigidity. A loss in transmission from a tight joint to a loose one is expected, but the presented results show the test method is capable of detecting an intermediate range of energy loss. This means that the test method presented can detect how rigid a joint is. Although different sensor pairings result in different values of the energy parameter  $E_r$ , a single sensor pair could be used to show changes in joint rigidity.

Results also showed that vibrating the spacecraft between measurements does not significantly affect the readings between identical configurations. This is indicative of the targeted nature of the test. Both PnP 1 experiments showed that the test technique was able to detect the relative torque on a bolt with repeatability of 5.7% when using an appropriate integrator gate width for the region of interest. The first phase of the experiment also showed that the gate width setting is important in improving the sensitivity and the repeatability of the measurement. Other factors that influenced the sensitivity of the test to indicate loose bolts included the method used to bond the sensors to the panel and different sensor paths.

The Experiment conducted on the PnP2 panels showed that the test could detect a loss of preload as small as 0.05 Nm if that bolt was in the direct path of the transmitted wave. The horizontal range for a single sensor pair was determined to be +/- 3 cm. Results also show that the assessment method is repeatable within 7% for a few bolt adjustments, but is not repeatable for larger numbers of adjustments.

PnP 2 tests suggest that the quality assessment metric could be improved to have a higher fidelity with appropriate equipment settings. Although repeatability was a

consideration and not a target of the experiments performed on PnP1, the lower repeatability values found in the PnP1 experiments are also indicative that improvement could be made.

### **6.3. Future work**

Results of both PnP 1 and PnP 2 experiments indicate that, for a given structure, there is an optimum frequency range and time window. Optimizing testing parameters would also go a long way to improving the repeatability and sensitivity of the test. It would be useful to investigate the affect of test parameters on several different joint geometries. An investigation into other factors that might influence the test result, like temperature and humidity changes, would also be useful.

The repeatability studied in this research only considered tests conducted on one specimen. In order to show that this assessment method is repeatable for assembly, the repeatability should be tested on several joint specimens with new bolts. As a factor in the repeatability for newly assembled parts, an investigation into the correlation with roughness due to common machining techniques used in satellite production and wave energy transmission should be performed.

An array of sensors placed near the joint would improve repeatability by providing a more complete picture of the joint by providing information at different angles and different locations across the joint. As transducers, the sensors could be excited in different patterns of succession. As sensors, the array could also further localize the source of damage. Larger brackets like the ones on PnP2 would benefit from a larger coverage area.

## REFERENCES

1. *Responsive Satellites and the Need for Structural Health Monitoring*. **Arritt, B.J., Buckley, S.J., Ganley, J.M., Kumar, A., Clayton, E.H., Hannum, R., Todd, M.D., Kennel, M.B., Welsh, J., Beard, S., Stabb, M.C., Xinlin, Q. and Wegner, P.** 2007, Proceedings of the SPIE, Vol. 6531, pp. 6531-6509.
2. **MIL-HDBK-340A**. *Test Requirements for Launch, Upper-Stage, and Baselines: Vol I and II*. s.l. : Department of Defense Handbook, 1985. DOD-HDBK-343, GSFC-STD-7000.
3. **Cheeke, J. David N.** *Fundamentals and Applications of Ultrasonic Waves*. Boca Raton : CRC Press, 2002. 0-8493-0130-0.
4. *Ultrasonic NDE of adhered T-joints using Lamb waves and intelligent signal processing*. **Challis, R.E., Bork, U. and Todd, P.C.D.** 2-5, October 1996, Ultrasonics, Vol. 34, pp. 455-459.
5. *Ultrasonic Guided Wave Inspection of Adhesive Joints: a Parametric Study for a Step-Lap Joint*. **Puthillath, Padma Kumar, et al.** s.l. : AIP Conference Proceedings, 2009. Proceedings of the 35th Annual Review of Progress in Quantitative Nondestructive Evaluation. Vol. 1096, pp. 1127-1133.
6. *Transmission and Reflection of A0 Mode Lamb Wave in a Plate Overlap*. **Song, Won-Joon, et al.** 2003. American Institute of Physics Conference Proceedings. Vol. 657, pp. 1088-1094.
7. *Damage detection in bolted space structures*. **Doyle, Derek, et al.** 2010, Journal of Intelligent Material Systems and Structures, Vol. 21, pp. 251-264.
8. *Damage assessment in a bolted lap joint*. **Lovell, P.A. and Pines, D.J.** San Diego CA : Society of Photo-Optical Instrumentation Engineers, Bellingham, WA, INTERNATIONAL, 1998. SPIE proceedings Smart systems for bridges, structures, and highways. Vol. 3325, pp. 112-126.
9. *The Use of Ultrasound in the Investigation of Rough Surface Interfaces*. **Dwyer-Joyce, R. S., Drinkwater, B. W. and Quinn, A. M.** 1, January 2001, Journal of Tribology, Vol. 123, pp. 8-16.
10. *Ultrasonic Scattering from Imperfect Interfaces: A Quasi-Static Model*. **Baik, Jai-Man and Thompson, R. Bruce.** 3/4, 1984, Journal of Nondestructive Evaluation, Vol. 4, pp. 177-196.

11. *Ultrasonic spectroscopy of imperfect contact interfaces between a layer and two solids*. **Lavrentyev, Anton I. and Rokhlin, S. I.** 2, February 1998, Journal of the Acoustical Society of America, Vol. 103, pp. 657-664.
12. *The Potential of Guided Waves for Monitoring Large Areas of Metallic Aircraft Fuselage Structure*. **Dalton, R. P., Cawley, P., and Lowe, M. S. J.** 1, 2001, Journal of Nondestructive Evaluation, Vol. 20, pp. 29-46.
13. *On Waves in an Elastic Plate*. **Lamb, Horace.** 648, s.l. : The Royal Society, March 01, 1917, Proceedings of the Royal Society of London. Series A, Containing Papers of a Mathematical or Physical Character, Vol. 93, pp. 114-128.
14. **Automation Creations, Inc.** Overview of materials for 6000 Series Aluminum Alloy. *Matweb Material Property Data*. [Online] [Cited: March 01, 2010.] <http://www.matweb.com/search/DataSheet.aspx?MatGUID=26d19f2d20654a489aefc0d9c247cebf&ckck=1>.
15. **Viktorov, I.A.** *Rayleigh and Lamb Waves: Physical Theory and Applications*. New York : Plenum Press, 1967. pp. 72, 67, 83. LCCN 67010537.
16. **Davis, Harry F. and Snider, Arthur David.** *Introduction to Vector Analysis*. Dubuque : Wm. C. Brown Publishers, 1991.
17. **Cady, Walter G.** *Piezoelectricity; an introduction to the theory and applications of electromechanical phenomena in crystals*. New York : Dover Publications, 1964. pp. 58,285,308,316. Vol. 1. LCCN 63017902.
18. **Uchino, Kenji.** *Ferroelectric Devices*. New York : Marcel Dekker, 2000. pp. 162,168. ISBN 0824781333.
19. *Embedded Non-destructive Evaluation for Structural Health Monitoring, Damage Detection, and Failure Prevention*. **Giurgiutiu, V. and Cuc, A.** 2, 2005, Vol. 37, pp. 83-105.
20. *Use of Lamb waves to monitor plates: Experiments and simulations*. **Greve, D.W, et al.** San Diego : s.n., 2005. Proceedings of the SPIE Smart Structures Conference. Vol. 5765, pp. 281–292.
21. *Generation and Detection of Guided Waves Using PZT Wafer Transducers*. **Nieuwenhuis, J.H., Neumann, J., Greve, D.W., Oppenheim, I.J.** 11, 2005, Vol. 52, pp. 2103-2111.
22. *Lamb Waves Generation in Plates Using Glued Piezoceramics*. **Gomez-Ullate, Y., Saletes, I. and De Espinosa, F. Montero.** 33, 2006, Boletin de la Sociedad Espanola de Ceramica y Vidrio, Vol. 45, pp. 188-191.

23. *Lamb Wave Generation with Piezoelectric Wafer Active Sensors for Structural Health Monitoring.* **Giurgiutiu, V.** 2003, Smart Structures and Materials 2003: Smart Structures and Integrated Systems, p. 111.
24. *Simulation and Testing of Transducers for Lamb Wave Generation.* **Niewenhuis, J.H., et al.** Orlando : s.n., 2005. Proceedings of the 23rd International Modal Analysis Conference (IMAC XXIII). p. Paper no. 216.
25. **Bray, Don E. and Stanley, Roderic K.** *Nondestructive Evaluation: A Tool in Design, Manufacturing, and Service.* Boca Raton : CRC Press, Inc., 1997. ISBN 0849326559.
26. *The response of rectangular piezoelectric sensors to Rayleigh and Lamb ultrasonic waves.* **Di Scalea, Francesco Lanza, Matt, Howard and Bartoli, Ivan.** 1, 2007, Journal of the Acoustical Society of America, Vol. 121, pp. 175-187.
27. *Reflection of the S0 Lamb Mode from a Part-Depth Circular Defect in a Plate, When the Incident Wave is Created by a Small Source.* **Diligent, O., Lowe, M. J. S., Cawley, P., Wilcox, P.** 2003. American Institute of Physics Conference Proceedings. Vol. 657, pp. 197-204.
28. *Boundary Element Modeling for Guided Wave Reflection and Transmission Factor Analyses in Defect Classification.* **Rose, J.L., Zhu, Wenhao and Cho, Y.** 1998. IEEE Ultrasonics Symposium Proceedings, . Vol. 1, pp. 885–888.
29. *Lamb mode conversion at edges: A hybrid boundary element–finite element solution.* **Galan, Jose M., Abascal , Ramon.** 4 Pt 1, 2005, Journal of the Acoustical Society of America, Vol. 117, pp. 1777-1784.
30. *Lamb wave reflection at the free edge of a plate.* **Morvan, Bruno, et al.** 3, 2003, The Journal of the Acoustical Society of America, Vol. 113, pp. 1417-1425.
31. *A boundary element solution for a mode conversion study on the edge reflection of Lamb Waves.* **Rose, Younho Cho and Joseph L.** 1996, Journal of the Acoustical Society of America, Vol. 99, pp. 2097-2109.
32. *Study of Lamb waves based upon the frequency and angular derivatives of the phase of the reflection coefficient.* **Lenoir, O. and Duclos, J.** 1, 1993, The Journal of the Acoustical Society of America, Vol. 94, pp. 330-343.
33. *Joint rigidity assessment with piezoelectric wafers and acoustic waves.* **Montoya, Angela C and Maji, Arup K.** 2009. 36th Annual Review of Progress in Quantitative Nondestructive Evaluation July 26-31. accepted for publication.

34. *Ultrasonic Classification of Imperfect Interfaces*. **Nagy, Peter B.** 3/4, 1992, Journal of Nondestructive Evaluation, Vol. 11, pp. 127-139.
35. *Ultrasonic Wave Scattering from Rough, Imperfect Interfaces. Part II. Incoherent and Coherent Scattered Fields*. **Pecorati, Claudio, Mendelsohn, Daniel A. and Adler, Laszlo.** 3, 1995, Journal of Nondestructive Evaluation, Vol. 14, pp. 117-126.
36. *Ultrasonic Wave Scattering from Rough, Imperfect Interfaces. Part I. Stochastic Interface Models*. **Pecorati, Claudio, Mendelsohn, Daniel A. and Adler, Laszlo.** 3, 1995, Journal of Nondestructive Evaluation, Vol. 14, pp. 109-116.
37. *Empirical rheological model for rough or grooved bonded interfaces*. **Vlasie Belloncle, Valentina and Rousseau, Martine.** 1-4, December 2007, Ultrasonics, Vol. 47, pp. 10-14 .
38. *Ultrasonic rheological model of cohesive and adhesive zones in aluminum joints: validation by mechanical tests* . **Vlasie, V., et al.** 4-5, February 2, 2006, Archive of applied mechanics, Vol. 75.
39. *Acoustical validation of the rheological models for a structural bond*. **Vlasie, Valentina and Rousseau, Martine.** 4, April 2003, Wave Motion, Vol. 37, pp. 333-349 .
40. *Mechanical and acoustical study of a structural bond: comparison theory/numerical simulations/experiment* . **Vlasie, Valentina, et al.** 3, May-June 2006, European Journal of Mechanics - A/Solids, Vol. 25, pp. 464-482 .
41. *Finite elements methods for modeling the guided waves propagation in structures with weak interfaces*. **Hosten, Bernard and Castaings, Michel.** 2005, Journal of Acoustical Society of America, Vol. 117(3), pp. 1108-1113.
42. *Sound Transmission Through Simply Supported Finite Double-Panel Partitions With Enclosed Air Cavity*. **Xin, F. X., Lu, T. J. and Chen, C. Q.** 1, February 2010 , Journal of Vibration and Acoustics, Vol. 132, p. 011008 (11 pages).
43. **A.C. Ugural, S.K. Fenster.** *Advanced Strength and Applied Elasticity*. New York : American Elsevier, 1975. 0-444-00160-3.
44. *The interaction of oblique incidence ultrasound with rough, partially contacting interfaces*. **Liaptsis, D., Drinkwater, B. W. and Thomas, R.** 3 and 4, 2006, Nondestructive Testing and Evaluation, Vol. 21, pp. 109-121.
45. *Wave scattering analysis of bolted joints*. **Miller, David, et al.** 2006. Proceedings of the SPIE: Nondestructive Evaluation and Health Monitoring of Aerospace Materials, Composites, and Civil Infrastructure . Vol. 6176, pp. 23-31.

46. *Parametric identification of a transmission line model for in situ damage characterization in lap joints.* **Francoeur, D., Micheau, P. and Masson, P.** 4, 2009, Smart Materials and Structures, Vol. 18, p. 045005 (12 pp.).
47. *Adaptive multi-analysis strategy for contact problems with friction. Application to aerospace bolted joints.* **Champaney, L., Boucard, P.-A. and Guinard, S.** 2, July 2008, Computational Mechanics, Vol. 42, pp. 305-315.
48. **APC International, Ltd.** *Piezoelectric Ceramics: Principles and Applications.* Mackeyville : APC Products Inc, 2002. pp. 15-18. ISBN 0-9718744-0-9.
49. **Hibbeler, R.C.** *Structural Analysis.* sixth. Upper Saddle River : Pearson Prentice Hall, 2006.
50. **Deshpande, J.V., Gore, A.P. and Shanubhoque, A.** *Statistical Analysis of Non-normal Data.* New York : John Wiley & Sons , 1995.
51. **Barrett, Richard T.** Fastener Design Manual. *NASA Reference Publication 1228.* 1990.
52. **Piezo Systems, Inc.** PIEZOCERAMIC MATERIALS & PROPERTIES. *Piezo Systems, Inc.* [Online] [Cited: March 1, 2010.] <http://www.piezo.com/prodmaterialprop.html>.
53. **Fishbane, Paul, Gasiorowicz, Stephen and Thornton, Stephen.** *Physics for Scientists and Engineers.* Second, extended. Upper Saddle River : Prentice Hall, 1996.
54. **RITEC Inc.** *RITEC RAM 5000 Specifications.*



# APPENDIX 1: Mathematica code used to produce Lamb wave dispersion curves

## Lamb dispersion relations in aluminum

This program's purpose is to find the lamb wave dispersion relations with Mathematica's numeric solver FindRoot. FindRoot will only find one root closest to a 'seed' that is specified by the user. Only the first four modes were solved for with this method, up to a frequency - thickness product of 5.

by Angela Montoya, July 2008. Revised : Feb  
.2010

Define the wave speeds in the longitudinal and  
transverse directions.

---

```
Clear[G, ξ, ζ, n, λ, Clong, Ctrans,  
antiSymCharEqn, symCharEqn];  
Clong = ((λ + 2 * G) / density)1/2;  
Ctrans = (G / density)1/2;
```

The parameter  $\xi$ , as defined by Viktorov. The parameter  
only depends on n, the value of Poisson's ratio.

---

```
ξ = √((Ctrans2 / Clong2));  
Solve[n == λ / (2 * λ + 2 * G), λ];  
ξ = ξ /. λ → - $\frac{2 G n}{-1 + 2 n}$  /. n → 0.330;
```

Define the symmetric and antisymmetric characteristic equations.

---

- $\zeta$  is defined as  $\zeta^2 = (\text{transverse wave speed})^2 / (\text{lambwave phase speed})^2$   
 $\text{dbar}$  is defined as  $\text{dbar} = \text{transverse wave number} * \text{the half thickness}$

```

symCharEqn[ $\zeta$ _, dbar_] :=
  (Tan[(1 -  $\zeta^2$ )1/2 * dbar]) /
  (Tan[( $\xi^2$  -  $\zeta^2$ )1/2 * dbar]) +
  (4 *  $\zeta^2$  * (1 -  $\zeta^2$ )1/2 * ( $\xi^2$  -  $\zeta^2$ )1/2) / (2 *  $\zeta^2$  - 1)2
antiSymCharEqn[ $\zeta$ _, dbar_] :=
  (Tan[(1 -  $\zeta^2$ )1/2 * dbar]) /
  (Tan[( $\xi^2$  -  $\zeta^2$ )1/2 * dbar]) +
  (2 *  $\zeta^2$  - 1)2 / (4 *  $\zeta^2$  * (1 -  $\zeta^2$ )1/2 * ( $\xi^2$  -  $\zeta^2$ )1/2)

```

This block of code loops through the symmetric equation numerically solving for the normalized phase velocity at different values of dbar.

---

- This section is intended to find values belonging in the first symmetric mode only. The seed used to numerically find this section of the solution is 0.6 and increases by 0.05 when FindRoot returns a value that does not belong to this mode. The results are stored in an array.

```

Clear[symPoints0, a];
Array[symPoints0, 100];
a = .6;
Do[
  Clear[c, dbar];
  c[a_] := FindRoot[{0 == symCharEqn[ $\zeta$ , i * .05]},
    { $\zeta$ , a}, MaxIterations -> 100];
  a = If[Re[1 / Part[c[a], 1, 2]] >= 1, a, a + .05];
  symPoints0[i] =
    {i * .05, Re[1 / Part[c[a], 1, 2]]};
, {i, 1, 100}]

```

This block of code loops through the symmetric equation numerically solving for for the normalized phase velocity at different values of dbar.

---

- This section is intended to find values belonging in the second symmetric mode only. It starts looking for values around (frequency - thickness product ) dbar = 2. The seed used to numerically find this section of the solution is 0.65 and increases (more slowly) by 0.005 when FindRoot returns a value that does not belong to this mode.

```
Clear[symPoints1, a];
Array[symPoints1, 50];
a = .65;
Do[
  Clear[c, dbar];
  c[a_] := FindRoot[{0 == symCharEqn[ $\zeta$ , i * .05]},
    { $\zeta$ , a}, MaxIterations -> 100];
  a = If[Re[1 / Part[c[a], 1, 2]] >= 1, a,
    a + .005];
  symPoints1[i - 49] =
    {i * .05, Re[1 / Part[c[a], 1, 2]]};
, {i, 50, 100}]
```

This block of code loops through the symmetric equation numerically solving for for the normalized phase velocity at different values of dbar.

---

- This section is intended to find values belonging in the first antisymmetric mode only. The seed used to numerically find this section of the solution is 0.1 and increases by 0.5 when FindRoot returns a value that does not belong to this mode.

```
Clear[antiSymPoints0, a];
Array[antiSymPoints0, 100];
a = .1;
Do[
  Clear[c, dbar];
  c[a_] :=
    FindRoot[{0 == antiSymCharEqn[ $\zeta$ , i * .05]},
    { $\zeta$ , 1.2}, MaxIterations -> 100];
  a = If[Re[1 / Part[c[a], 1, 2]] >= .001, a,
    a + .5];
  antiSymPoints0[i] =
    {i * .05, Re[1 / Part[c[a], 1, 2]]};
, {i, 1, 100}]
```

This block of code loops through the symmetric equation numerically solving for for the normalized phase velocity at different values of  $dbar$ .

---

- This section is intended to find values belonging in the second antisymmetric mode only. The seed used to numerically find this section of the solution is 0.2 and increases by 0.1 when FindRoot returns a value that does not belong to this mode.

```
Clear[antiSymPoints1, a];
Array[antiSymPoints1, 60];
a = .2;
Do[
  Clear[c, dbar];
  c[a_] :=
    FindRoot[{0 == antiSymCharEqn[ $\zeta$ , i * .05]},
      { $\zeta$ , a}, MaxIterations → 100];
  a = If[Re[1 / Part[c[a], 1, 2]] ≥ .001, a,
    a + .1];
  antiSymPoints1[i - 39] =
    {i * .05, Re[1 / Part[c[a], 1, 2]]};
  , {i, 40, 100}]
```

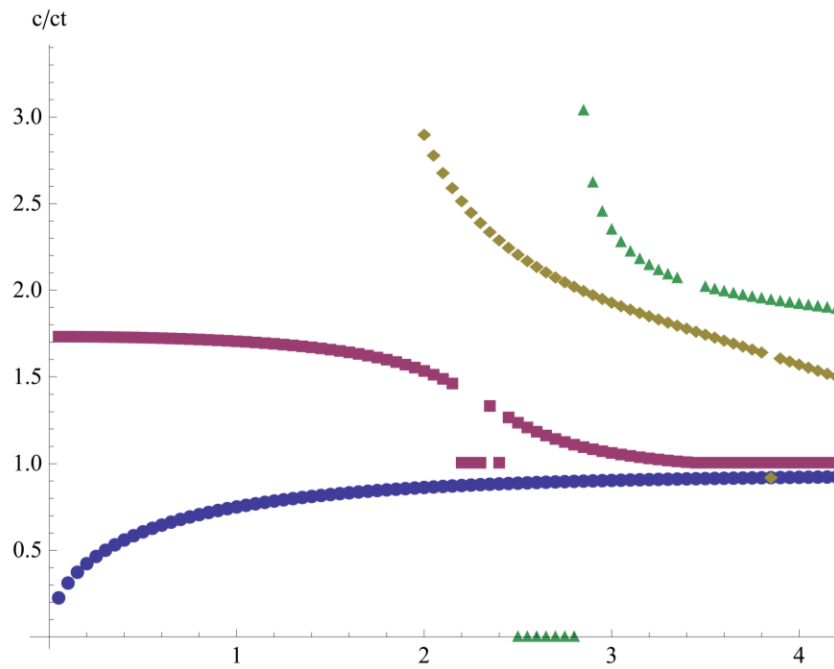
Plot of results.

---

- Blue is the first anti - symmetric mode, purple is the first symmetric mode, yellow is the second anti - symmetric mode, and green is the second symmetric mode.

```
ListPlot[{Array[antiSymPoints0, 100],
  Array[symPoints0, 100],
  Array[antiSymPoints1, 60],
  Array[symPoints1, 50]},
  AxesLabel → {"kt*d", "c/ct"},
  PlotLabel →
    "Dispersion Curves for Aluminum (Poisson's
    ratio of 0.33)",
  PlotMarkers → {Automatic, Small}]
```

Dispersion Curves for Aluminum (Poisson's ratio of 0.33)



The values found by this program were exported to text files. This was done so that a cleaner plot could be made in MatLab.

```
Export ["antiSymPoints0.txt",
  Array[antiSymPoints0, 100]]
Export ["antiSymPoints1.txt",
  Array[antiSymPoints1, 60]]
Export ["symPoints0.txt", Array[symPoints0, 100]]
Export ["symPoints1.txt", Array[symPoints1, 50]]
```

antiSymPoints0.txt

antiSymPoints1.txt

symPoints0.txt

symPoints1.txt

## APPENDIX 2: Material data for PiezoSystems PSI-5A4E (51)

Piezo Systems' Designation		PSI-5A4E	PSI-5H4E
Industry Designations		Navy type II; Industry Type 5A	Navy type VI; Industry Type 5H
Composition		Lead Zirconate Titanate	Lead Zirconate Titanate
Relative Dielectric Constant (@ 1 KHz)	$K^T_3$	1800	3800

**Piezoelectric "d" coefficients relate the Strain Produced / Electric Field Applied or the Short Circuit Charge Density Produced / Stress Applied**

$d_{33}$	meter/Volt or Coulomb/Newton	$390 \times 10^{-12}$	$650 \times 10^{-12}$
$d_{31}$	meter/Volt or Coulomb/Newton	$-190 \times 10^{-12}$	$-320 \times 10^{-12}$

**Piezoelectric "g" coefficients relate the Open Circuit Electric Field Produced / Stress Applied or the Strain Produced / Charge Density Applied**

$g_{33}$	Volt-meter/Newton or meter <sup>2</sup> /Coulomb	$24.0 \times 10^{-3}$	$19.0 \times 10^{-3}$
$g_{31}$	Volt-meter/Newton or meter <sup>2</sup> /Coulomb	$-11.6 \times 10^{-3}$	$-9.5 \times 10^{-3}$

### Electrical properties

Coupling Coefficient	$k_{33}$		0.72	0.75
	$k_{31}$		0.35	0.44
Polarizing Field	$E_p$	Volt/meter	$> 2 \times 10^6$	$> 1.5 \times 10^6$
Initial Depolarizing Field	$E_c$	Volt/meter	$\sim 5 \times 10^5$	$\sim 3 \times 10^5$
Coercive Field	$E_c$	Volt/meter	$\sim 1.2 \times 10^6$	$\sim 8 \times 10^5$

### Mechanical properties

Density	$\delta$	Kg/meter <sup>3</sup>	7800	7800
Mechanical Q			80	32
Elastic Modulus	$Y^E_3$	Newton/meter <sup>2</sup>	$5.2 \times 10^{10}$	$5.0 \times 10^{10}$
	$Y^E_1$	Newton/meter <sup>2</sup>	$6.6 \times 10^{10}$	$6.2 \times 10^{10}$

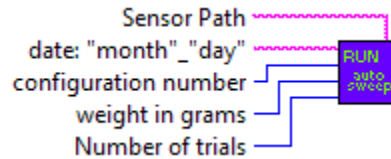
### Thermal properties

Thermal Expansion Coefficient		meter/meter °C	$\sim 4 \times 10^{-6}$	$\sim 3 \times 10^{-6}$
Curie Temperature		°C	350	230

## APPENDIX 3: Documentation for LabView programs

### Proof of Concept Data Collection Programs:

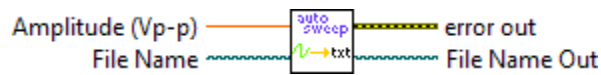
#### Run Auto\_Frequency\_Sweep V4.vi



This program was used as the master routine. It creates folders and names for data. It runs a specified number of trials for each input voltage (1.0, 2.0, and 3.0 volts) and calls on Auto\_Frequency\_Sweep V4.vi for each trial.

By A. Montoya October, 2008

#### Auto\_Frequency\_Sweep V4.vi

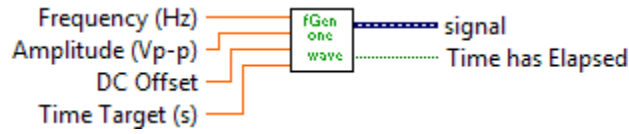


The primary purpose of this program is to loop through frequency values, and run FGen user defined modified.vi for each frequency value and save the resulting array to a text file. This program will also output graphic displays of the output and calculate the maximum amplitude for the data set.

By A. Montoya October, 2008



### Fgen user defined modified.vi



Function generator program from National Instruments. It creates a sine wave train for a specified number of seconds and records the output at the digitizer with NI-Scope Express.

Modified by A. Montoya July 2008

### Proof of Concept Data Analysis Programs

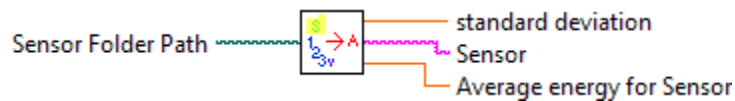
#### Report avg area data on config number folder.vi



This program gets a folder path that contains sensor path folders. It calls Sensor Folder to avg area.vi and reports the results for each folder in a string.

By A. Montoya January 2009

#### Sensor Folder to avg area.vi



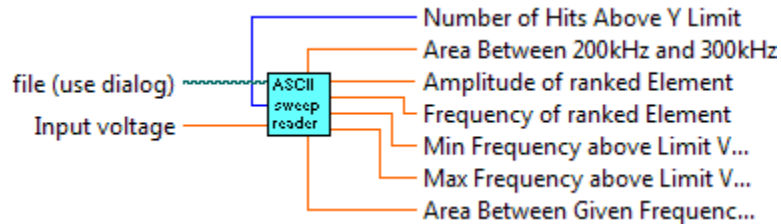
This program takes the path to a Sensor folder and loops to find each file. It calls on get average area data from folder.vi to get the average  $E_j$  value for each input voltage. Then all (in this case 9) files are averaged. It also computes the standard deviation for the folder.

### get average area data from folder.vi



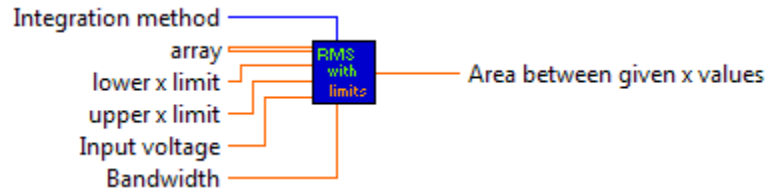
This program takes a folder path that contains files at the same input voltage. It parses out the file names and correctly passes the input voltage based on the name to ASCII Sweep Reader V2.vi. The resulting array of normalized  $E_j$  values is averaged and reported as “average area”. This program contains options to report the raw data without averaging and without dividing by the input voltage.

### ASCII Sweep Reader V2.vi



This program pulls data out of a text file, and reports the "Area Between 200 kHz and 300 kHz" by calling on RMS energy method between limits.vi. Other functions of this program were intended to examine features of the data by hand.

## RMS energy method between limits.vi

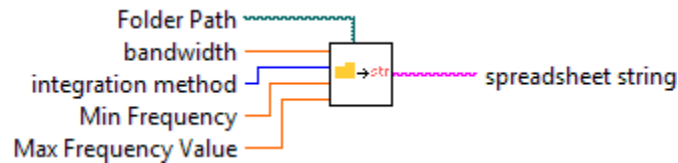


This program takes a data array that contains amplitudes and input frequencies. Divides the amplitude by the input voltage, squares the result, divides by the bandwidth (in this case 1.0), and then integrates the resulting array with the specified rule.

By A. Montoya January 2009

## PnP 1 and PnP 2 LabView Data Analysis Programs

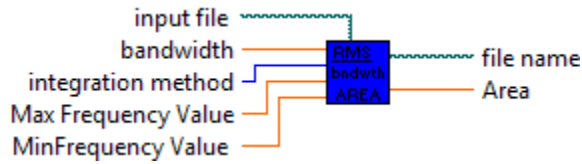
### Get energy values for folder into string.vi



This program was used as the master routine. It took a folder containing data files and called RMSoverBandwith Area.vi for each file. The resulting array was formatted into a string that matched the file name with the “E” values associated with it.

By A. Montoya August, 2009

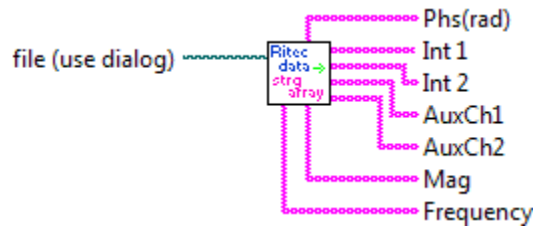
### RMSoverBandwidth Area.vi



This program took a data file and parsed the text into a string array by calling Ritec Data to String Array.vi. The string arrays were then converted to data type 'double'. The amplitudes for each frequency were squared, divided by the bandwidth (in this case 1), and integrated with the chosen integration method. This program was also able to find E values for specific ranges in the data set. The output variable "Area" is E.

By A. Montoya August, 2009

### Ritec Data to String Array.vi



This program parses the text file into string arrays.

By A. Montoya August, 2009

## APPENDIX 4: Derivation of joint rigidity equation

The motion in the vertical plane is depicted below in Figure 30. For brevity, only one beam is shown. The initial plate position (plate position 1) is vertical in reference to the floor. The beam is level with the floor. Initially, the beam strikes the plate and reflects onto the screen in the same vertical position. This location is recorded on the screen.

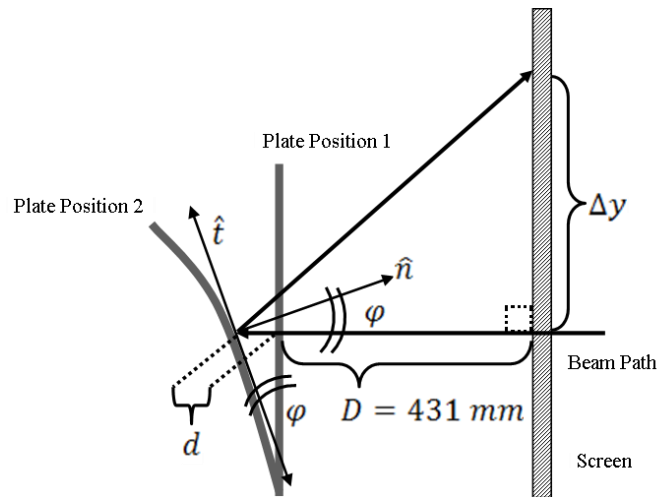


**Figure 30: View of the vertical plane. The bend in the vertical plate moves the reflected beam from a horizontal position on the screen to some higher point. The change in position is denoted  $\Delta y$ .**

When the plate is loaded, it will bend (plate position 2). The beam will reflect off the normal at that location, according to the laws of reflection (52), at an angle equal to the incident angle  $\phi$ . As shown in Figure 30, this angle is also equal to the angle the tangent makes with the vertical. Knowing  $\Delta y$ ,  $D$ , and  $d$ ,  $\phi$  can be found. Looking at Figure 30, a right triangle is formed by  $\Delta y$  and the distance to the point of interest. That relationship is summarized in Equation 23.

$$\tan 2\varphi = \frac{\Delta y}{d + D}$$

The values  $\Delta y$  and  $D$  are known. All that remains is to extract  $d$  from  $\Delta x$ . The horizontal motion of the plate is shown in Figure 31 and Figure 32.

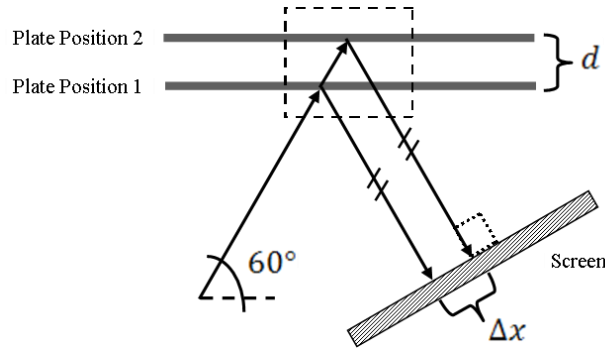


**Figure 31: Horizontal plane, top-down view. As the plate changes position, the incident angle does not change. However, the change in position shifts the reflected beam by some distance  $\Delta x$ .**

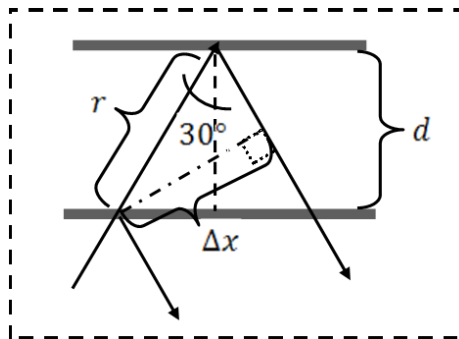


**Figure 32: Close in view of the horizontal plane. Here, the geometry is more obvious. The outgoing beams are parallel, so the perpendicular distance between them is  $\Delta x$ , all along the length of the beams. Choosing a distance  $\Delta x$  that intersects the origin of the original outgoing beam, a right triangle is created that contains the distance  $r$ . The distance  $r$  is also contained in the right triangle that contains  $r$  and the distance between the plates  $d$ .**

From Figure 32, two right triangles are formed. The first one contains  $r$ ,  $d$ , and the angle of incidence  $30^\circ$ . The beam is oriented at  $60^\circ$  from the horizontal (as viewed in

figure A.3.2). It strikes the plate at an incident angle of  $30^\circ$  with respect to the normal. The resulting  $30^\circ/60^\circ$  right triangle leads to the following relationship between  $r$  and  $d$ :

$$\frac{\sqrt{3}}{2} = \frac{d}{r} \quad 24$$

The second triangle contains  $\Delta x$ ,  $r$ , and twice the incident angle. The resulting  $60^\circ/30^\circ$  right triangle leads to the following relationship between  $\Delta x$  and  $r$ :

$$\frac{\sqrt{3}}{2} = \frac{\Delta x}{r} \quad 25$$

Combining Equations 24 and 25, leads to  $\Delta x = d$ . The incident angle of  $30^\circ$  was specifically chosen to maximize the relationship between  $\Delta x$  and  $d$ . Substituting  $\Delta x$  for  $d$  in Equation 23, the final relationship between  $\Delta x$ ,  $\Delta y$ , and  $\phi$  is given by Equation 17.

## APPENDIX 5: Summary of Ritec documentation for the integrator circuit

The RITEC RAM 5000™ uses a series of analogue circuits to filter and process high frequency, high voltage signals (53). For each burst sent to the actuating sensor, a response is read into the RITEC RAM 5000 from the receiving sensor. The response is filtered to the burst frequency and then passed through two circuits that split the signal into two orthogonal vector components (labeled  $D_1$  and  $D_2$  in the equations below). A gate is specified by the user by a delay time and a length (or width). The gate is used as the limits for the following integrations:

$$I_1 = r \int_{t_1}^{t_2} D_1(t) dt = \int_{t_1}^{t_2} A(t) \cos \varphi dt \quad 26$$

$$I_2 = r \int_{t_1}^{t_2} D_2(t) dt = \int_{t_1}^{t_2} A(t) \sin \varphi dt \quad 27$$

The variable  $t$  is time,  $\varphi$  is the phase angle,  $A$  is the amplitude,  $r$  is the integrator rate, and the outputs are  $I_1$  and  $I_2$ . The amplitude is then found by combining the components  $I_1$  and  $I_2$ .

$$A = \sqrt{I_1^2 + I_2^2} \quad 28$$

The integration rate,  $r$ , is user specified. This value is usually set high enough to get a decent response, but low enough not to overload the circuit. It is important to note that the resulting amplitude is scaled by  $r$ . In all experiments done for this thesis, care was taken to ensure that the same integrator rate was used for both baseline and variable cases. This way, the integrator rate canceled out of the ratio  $E_r$ .



For experiments described in Chapters 3 and 4 of this thesis, the reported amplitude at each frequency value is an average of at least three trials. Five trials was tried first, but no appreciable difference in signals between 3 and 5 averages could be found after the equipment was allowed to warm up.

## APPENDIX 6: Panel and bracket dimensions for PnP 2

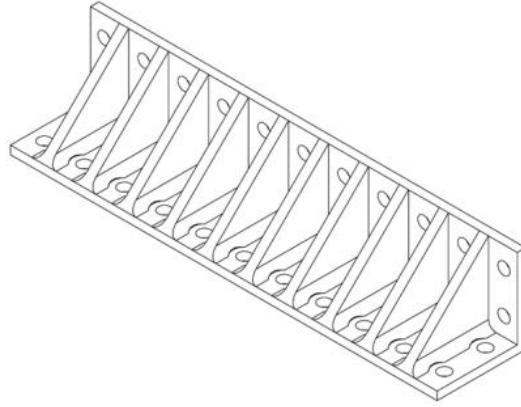


Figure 33: PnP 2 Bracket geometry

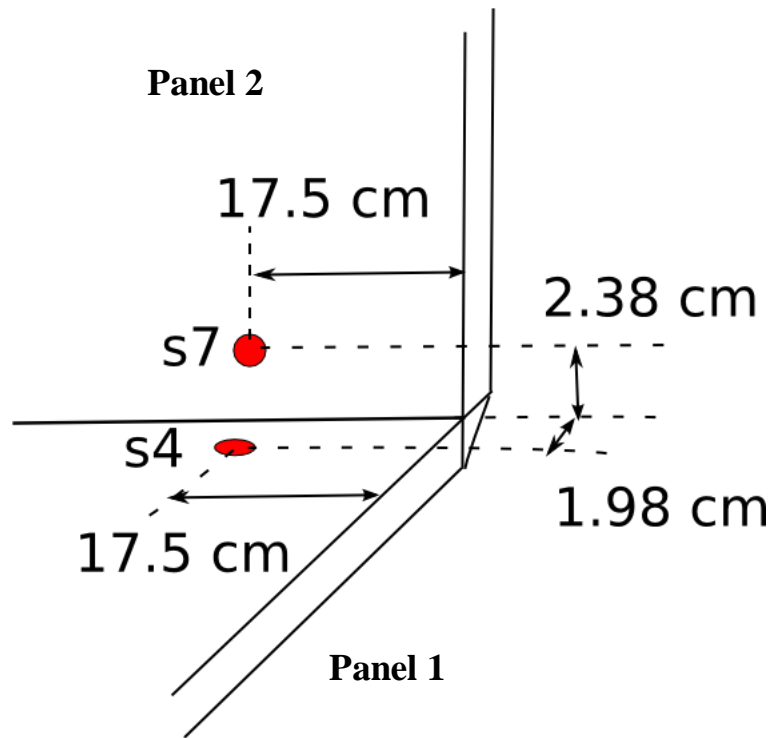


Figure 34: Sensors placed near bracket 1. Red dots indicate sensors.